©Copyright 2025
Grace Dojan

Static Response and Failure Analysis of Anisotropic Parts Printed using Fused Filament Fabrication

Grace Dojan

A dissertation submitted in partial fulfillment
of the requirements for the degree of

Master of Science

University of Washington

2025

Committee:

Richard Wiebe

Marco Salviato

Program Authorized to Offer Degree:
Civil and Environmental Engineering

University of Washington

Abstract

Static Response and Failure Analysis of Anisotropic Parts Printed using Fused Filament Fabrication

Grace Dojan

Chair of the Supervisory Committee:
Richard Wiebe
Civil and Environmental Engineering

Additively manufactured polymer parts produced via Fused Filament Fabrication (FFF) exhibit direction-dependent behavior as a result of the deposition process. This anisotropy presents a challenge for aerospace applications, where material properties and failure mechanisms vary depending on the orientation of the material. To accurately model and anticipate the behavior of Poly-Ether-Ether-Ketone (PEEK), a high-strength and high-temperature thermoplastic, this study explored strain limit failure mechanics. Uniaxial tension tests were performed on custom-dimensioned PEEK dogbone coupons across multiple material orientations and print rasters. Digital Image Correlation enabled full-field strain measurement across coupon surfaces and a "Strain Tornado" method was developed to interpret locally oriented strains. This analysis revealed the orientation-dependent strain limits and failure trends both between different material orientations and between FFF print rasters. A MATLAB Finite Element program was developed, incorporating transverse isotropy to predict anisotropic material behavior. Beam case studies explored this strain-based approach for flexural loading. These results establish the foundation for reliable strain-based design methods, building design confidence of 3D-printed PEEK in aerospace applications.

TABLE OF CONTENTS

Page

List of Figures iii

Glossary v

Chapter 1: Introduction 1
1.1 Motivation 1
1.2 Background 1
1.3 Scope 6

Chapter 2: Experimental Design and Methods 7
2.1 Specimen Design 7
2.2 Sample Preparation 7
2.3 Testing 12

Chapter 3: Model Development 15
3.1 Transversely Isotropic Model 15
3.2 Matlab Code 16

Chapter 4: Results 21
4.1 Post-Testing Coupon Images 21
4.2 Printer Consistency Verification 22
4.3 Strain and Hotspot Analysis 23
4.4 FEA Output and Discussion 31

Chapter 5: Case Study 44
5.1 Motivation 44
5.2 Design 44
5.3 Experimental Process 44
5.4 Results 45

Chapter 6: Future Work 51
6.1 Study Expansion 51
6.2 3D Strain Tornadoes 51
6.3 Geometry Expansion 51

Bibliography 54

Appendix A: Appendix A: GOM Strain Extraction 56

LIST OF FIGURES

Figure Number — Page

1.1 FFF extrusion nozzle diagram . . . 2
1.2 Top view of [± 45°] and [0°/90°] configurations . . . 3

2.1 Dimensions and appearance of the test coupon . . . 8
2.2 Printed blank and visualization of extraction . . . 9
2.3 Dimensions and appearance of flat and vertical Type V travelers . . . 9
2.4 The B-angle where fibers just span the coupon test length, $\approx B = 25.05°$ . . . 10
2.5 B-angle graphics . . . 12
2.6 Blank prints directly after routing . . . 13
2.7 Coupon without and with DIC tattoo paper . . . 13
2.8 Coupon testing setup . . . 14

3.1 Two possible FEA fixity configurations . . . 17
3.2 One-layer Wide coupon mesh (Left), two-Layer wide coupon mesh (Middle), one-Layer traveler coupon mesh (Right) . . . 18
3.3 Example of exported GOM data. The localized normal and shear strains as well as their corresponding coordinates would allow integration with the MATLAB FEA program. . . . 20

4.1 All tested PEEK dogbone coupons ([0/90] configuration) . . . 22
4.2 All tested PEEK dogbone coupons ([±45] configuration) . . . 23
4.3 $B = 25.05°$ coupon stress concentrations . . . 24
4.4 Stress-strain curves for all flat travelers . . . 24
4.5 Stress-strain curves for all vertical travelers . . . 25
4.6 Diagrams demonstrating untransformed global strains, transformed local strains, higher discretization of local strains, and extremely dense discretization of local strains, respectively. . . . 26
4.7 Coupon 46 at Step 1. . . . 28
4.8 Coupon 46 at Step 200. . . . 29
4.9 Coupon 46 at Step 416. . . . 30
4.10 Coupon 46 at Step 601. . . . 30

4.11 Coupon 46 at Step 628. 31
4.12 [±45] Raster, $B = 0°$ Tornado 32
4.13 [±45] Raster, $B = 15°$ Tornado 33
4.14 [±45] Raster, $B = 30°$ Tornado 34
4.15 [±45] Raster, $B = 45°$ Tornado 35
4.16 [±45] Raster, $B = 90°$ Tornado 35
4.17 [0/90] Raster, $B = 0°$ Tornado 36
4.18 [0/90] Raster, $B = 30°$ Tornado 37
4.19 [0/90] Raster, $B = 45°$ Tornado 37
4.20 [0/90] Raster, $B = 90°$ Tornado 38
4.21 Strain Tornado for all ±45 Coupons 39
4.22 Strain Tornado for all 0/90 Coupons 40
4.23 Sample FEA output for $B = 0°$ 41
4.24 Sample FEA output for $B = 15°$ 41
4.25 Sample FEA output for $B = 30°$ 42
4.26 Sample FEA output for $B = 45°$ 42
4.27 Sample FEA output for $B = 90°$ 43

5.1 Dimensions of the beam and prism used for the case Study 45
5.2 Theoretical cross section geometry needed for a failure due to established ϵ_{22} 45
5.3 Beam with DIC y-coordinates highlighted (pre-load) 46
5.4 Strain Tornado for [±45] prisms 47
5.5 Flexural stress-strain curves for the [±45] beams and prisms 48
5.6 Strain tornado for [0/90] prisms 49
5.7 Flexural stress-strain curves for the [0/90] beams and prisms 50

6.1 3d Strain Tornado for coupon 46 52

GLOSSARY

B-angle: The angle at which the filament deposition layers of a coupon are oriented relative to the printed angle. A $B = 0°$ coupon has deposited filament layers parallel to the tensile test direction, and a $B = 90°$ coupon has deposited filament layers perpendicular to the tensile test direction.

Blank: Used to name the 2.8mm x 116mm x 116mm element, printed with one of the 2.8mm x 116mm faces towards the print bed, also known as a placard.

DIC: Digital Image Correlation

FFF: Fused Filament Fabrication

FEA: Finite Element Analysis

PEEK: Poly-ether-ether-ketone

PEKK: Poly-ether-ketone-ketone

Prism: Name for geometry used in the beam case study- these samples are printed right rectangular shapes of dimensions 4x8x100 [mm].

Strain Tornado: Term that refers to the appearance of the plot generated by graphing measured strain points in local directions on the coupon surface until coupon failure.

Traveler: Name for the ASTM Type V coupons manufactured and extruded alongside the full-size test coupons, both vertically and horizontally with respect to the build plate- used to confirm consistency throughout the process.

Chapter 1
INTRODUCTION

1.1 Motivation

Additive manufacturing in aerospace applications has many advantages, including quick production speed, extreme ability to customize parts, and relatively low construction costs. The inherent anisotropy of the Fused Filament Fabrication (FFF) materials, however, can lead to unpredictable failure mechanisms. Because of this, modeling the material for structural design is often considered unreliable or inconsistent. The material of interest is Poly-Ether-Ether-Ketone (PEEK), a high-temperature and high-strength thermoplastic commonly used in injection-molded applications. This study aims to characterize these 3D-printed PEEK parts at a mesoscopic (the scale of interactions between deposited filaments [1]) lens for better predictability of failure through comprehensive uniaxial tensile testing by establishing baseline strain limits in each local material orientation. These strain limits can then serve as design aids for future print-direction-conscious material modeling in low-criticality aerospace components.

1.2 Background

This project is an expansion of prior work completed at the University of Washington, as seen in [2], to evaluate Fused Filament Fabrication PEEK polymer parts printed on an Intamsys FUNMAT HT printer,. Previously, there was a focus on specific bracket geometries and the development of characterization methods.

1.2.1 Fused Filament Fabrication

As shown in Figure 1.1, 3D FFF printers build parts one layer at a time with a nozzle traversing the x and y axes, while the printer head ascends along the z-axis at small increments, enabling the gradual buildup of extruded molten filament.

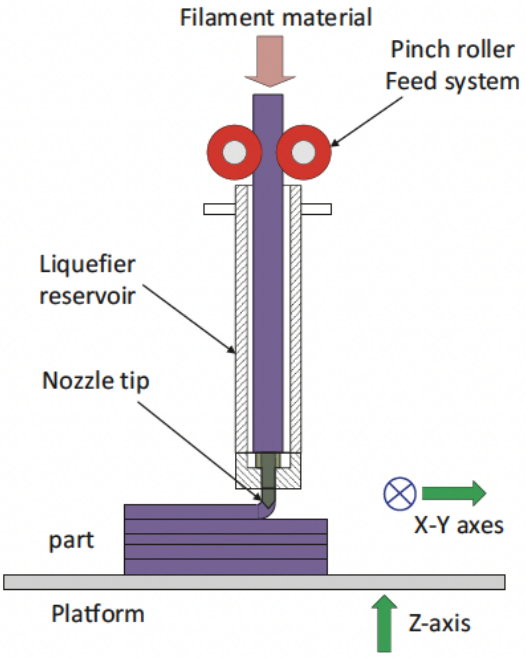


Figure 1.1: FFF extrusion nozzle diagram

Various deposition configurations exist to fill each layer. This path is called a raster pattern, and the path of the nozzle is called the tool path. Raster pattern is noted in [3] as one of the leading variables impacting FFF specimen strength. Two common raster patterns are [0°/90°] and [± 45°] configurations (top view illustrated in Figure 1.2), both widely-used tool paths in the industry with their alternating filament direction layouts. This investigation focuses on these two raster patterns to understand how varying the extruded filament lines within a layer affects the overall structural behavior of these parts.

Another element of deposition pattern to consider is concentric vs. line patterns. By default, many FFF printers use concentric patterns, in which the outermost outline of the part forms the basis for concentric outlines towards the middle of each layer. This is an efficient way to lay down material, as noted in [4]. For this study, line patterns- in which filament is extruded in unidirectional rows throughout each layer- was used to obtain consistent material properties through the thickness of the coupon.

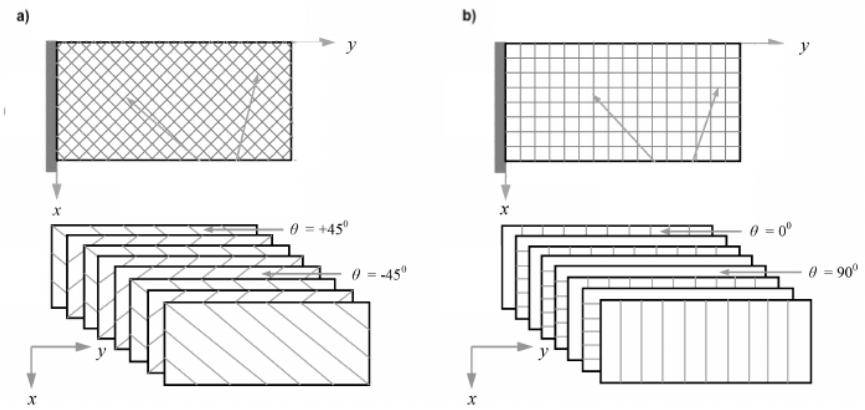


Figure 1.2: Top view of [± 45°] and [0°/90°] configurations

The variable out-of-plane behavior of FFF-printed materials comes from the manufacturing process. The extruded lines of filament tend to bond well within the layer because of the similarity of temperature and consistency of direction. But between layers, as molten filament is laid down and solidifies, similar bonding between extruded layers is never fully achieved. This bond is weaker due to lower temperatures and extended amount of time between contact with the material of the next extruded layer. When forces are applied to the material, the alignment of this force relative to extrusion lines is an important factor to consider. Parts where the extruded filament lines lie in the same direction as the applied force can take more load than parts where the force is applied in the z-direction of printing- the significantly weaker direction- and failure often begins along the layer lines. With all of the above factors, FFF partsa re highly anisotropic and have different mechanical behaviors depending on the orientation of the part and load application direction.

1.2.2 Anisotropy in Fused Filament Fabrication

Many studies have evaluated the strength of various print rasters under tensile loading parallel to the print plane. Studies such as [5] examine raster orientations and their perpendicularity's effects on material strength, through several methods of testing for FFF specimens. In a study closely aligned with this thesis' intended approach, [6], pure PEEK

strain was analyzed using DIC, although the tests were limited to flat printed coupons with a shell. A similar post-test DIC method with a shell was used in [7], where strain and failure propagation were studied in flat PLA coupons.

Inclusion of a shell, where at least one layer of filament outlines the layer's outermost shape, does help with minimizing print line discretization at the coupon radius for horizontally printed parts and therefore decreases stress concentrations as noted in [8]. However, as seen in [9], increasing the numbers of shells within a print directly increases the strength of the specimen. This effect is also examined thoroughly in [10], where varying print shell line amounts and performing subsequent tensile testing indicated higher moduli and strengths with greater numbers of shells. Consequently, this PEEK characterization study did not incorporate a shell during printing to maintain material homogeneity within each print layer and to keep testing both repeatable and potentially scalable for future expansions.

Anisotropic behavior in vertically (i.e. tensile testing direction perpendicular to print layers) printed PLA test coupons was examined in [11]. This study notes that directly and vertically printing these coupon shapes introduces variation in layer print times as the nozzle height increases. This is due to the inherent dogbone shape and taper, where some layers require different material amounts due to the changing geometry and thus take longer or shorter to move to the next layer. These print time differences cause variation in material properties through the coupon height.

In this research, a key goal is to characterize material behavior and predict failure thresholds at any possible printing orientation- not just horizontally or vertically printed coupons. The B-angle, often referred to as "B" in the following analysis, is the difference in angle between the printed fiber direction and actual intended test orientation of the coupon. Many studies have taken B-angle examination approaches similar to those shown in [12], where parts are printed at varying B-angles and then tested. While these methods are resource-efficient and provide a broad view of FFF behavior, there are still areas in the manufacturing process that could be improved. Specifically, they don't account for the variation in layer print times caused by extruding the support structures, and experience some of the previously noted material inconsistencies that come from directly vertically printing parts. Additionally, most of these studies focus on PLA or ABS, whereas our work

aims to characterize the behavior of pure PEEK.

In [1], compact tension tests of PLA were conducted both perpendicular and parallel to the print layer plane, and through a mesoscopic lens. By using two different raster patterns and both horizontal and vertical print orientations and Digital Image Correlation (DIC), anisotropic characteristics in FFF specimens became apparent.

1.2.3 Modeling Anisotropy

To move forward with material characterization, the aforementioned orientation considerations and anisotropic variation need to be taken into account. An orthotropic assumption for modeling FFF materials would accommodate the directional differences, but due to the orthogonal raster layout, two of these directions would theoretically end up with the same properties. Therefore, an initial assumption of transverse isotropy is useful for modeling these FFF parts and aligns with the expected physical behavior of the material. Transverse isotropy means that the in-plane strain directions share the same constitutive properties, while the out-of-plane direction (the vertical printing direction) has different properties. In-plane behavior differences would therefore depend only on the raster orientation, which is kept consistent across all specimens in this test setup at either [$\pm$ 45] or [0/90].

1.2.4 Digital Image Correlation

Taking inspiration from the aforementioned [1] and countless other studies, this examination of PEEK will also use DIC to view strain on the surface of the test subjects but employ dogbone coupons subjected to standard tensile tests instead of compact tension tests. In DIC, a speckled pattern, as seen in Figure 2.7, is applied to the test subject, then sequential pictures taken during testing are put into software that can optically track the pattern's deformation. After scaling to the coupon size and alignment of the coordinates to compensate for any non–orthogonal camera placements, DIC allows for comprehensive data extraction. This includes the strain from any point on the test subject where the DIC pattern was implemented and at any time step where images were captured during testing.

DIC was used in [13] to analyze three different horizontally printer Carbon-Fiber Rein-

forced PEEK (C-PEEK) rasters in tensile testing. The study highlighted strain concentrations at varying applied stresses for each of the rasters and analyzed the difference between samples, noting not only the strength that each sample exhibited but the largest strain each coupon saw before failure from DIC. Using strain to analyze more than just mechanical modulus strength is another way to quantify a material's expected behavior, and is a method to be expanded upon in this study.

1.3 Scope

This study used a new coupon geometry to examine the effects of FFF on material strain limits using consistent print layer times and purposive exploration of layer orientations. The PEEK FFF coupons are produced then tensile tested at multiple B-angle orientations. Coupon testing was completed to maximize DIC output for use in later evaluation. To complement the physical testing, a finite element analysis (FEA) was conducted to confirm the characterized elastic behavior and to help predict strain concentrations at extended orientations. The validity of these characterizations was then evaluated through a case study, in which beam and prism elements were produced and tested.

Chapter 2

EXPERIMENTAL DESIGN AND METHODS

This chapter explains the methods of this study used to observe the mechanical behavior of PEEK under tensile loading. The nature of 3D-printed material creates the need for specialized procedures and designs that exhibit the extremes of this material's direction-dependent performance under tensile loading. The following sections detail these procedures including custom coupon design, consistent printing and coupon extraction methods, DIC surface preparation, tensile testing approaches, and expected test output.

2.1 Specimen Design

Because of the need to investigate the material's anisotropy, a customized wide coupon was designed and used in this study, the dimensions of which can be seen in Figure 2.1. Validated in Finite Element Analysis and detailed in [2], this specified shape allows for a larger observation surface than most ASTM standard coupons, and minimizes stress concentrations to be below 1.02 at the tapered corners.. This value, which required an atypically large fillet radius, was chosen to increase the probability of breakage within the test sections while preserving surface area. In addition, the small grip length of the chosen geometry allows for more efficient use of material within the manufacturing procedure.

2.2 Sample Preparation

Prior to tensile testing, the coupons were prepared in stages including printing, coupon extraction, and test assembly in accordance with [2]. All PEEK sample manufacturing and preparation was completed between the UW's Mechanical Engineering printing room and Murdoch Lab, the Advanced Composites Center, and the Guggenheim Aerospace lab.

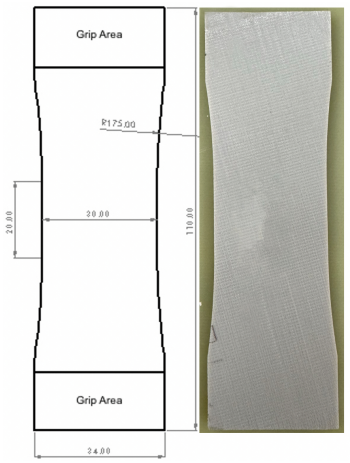


Figure 2.1: Dimensions and appearance of the test coupon

2.2.1 Printing

As mentioned in Section 1.2.2, directly printing the coupon shape would yield a part likely to experience the effects similar to other studies with vertically printed samples, particularly the varied consistency at which the layers bond through the z-direction. In addition, directly printing the shape requires supports and overhangs which amplify effects from inconsistent edge conditions between B-angles. As seen in Figure 2.2, blanks (also known as placards) of 116 x 116 x 2.8mm were printed, and then coupons were extracted in the desired orientation to ensure uniformity among the samples. Along with the blank, a flat ASTM type V traveler (dimensions in Figure 2.3) was printed every 3 blanks on the printer bed and tested later to ensure consistency in print quality. Equal amounts of blanks were produces in both rasters of [0°/90°] and [± 45°].

The PEEK blanks were produced using an Intamsys FUNMAT HT printer, and parameters were adjusted for to ensure optimal print quality and consistency, consistent with those seen in [2] . Printing was completed at a material extrusion temperature of $400°C$, the chamber temperature was 80° C, and the build plate temperature was kept at 160° C. Careful selection and monitoring of printing conditions resulting in parts in an opaque crystalline state rather than the translucent amorphous state that can come with higher

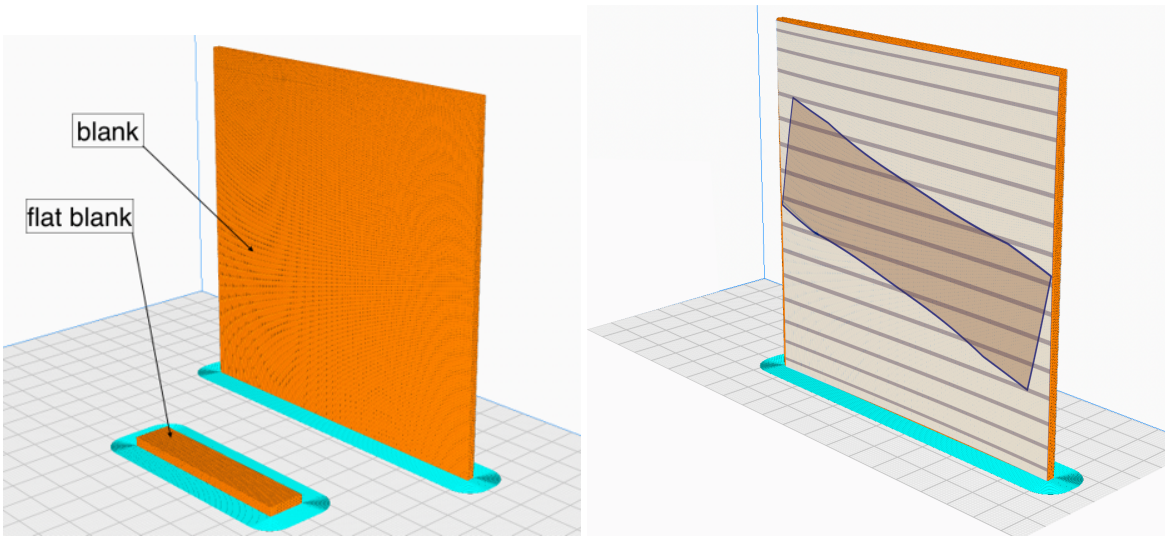


Figure 2.2: Printed blank and visualization of extraction

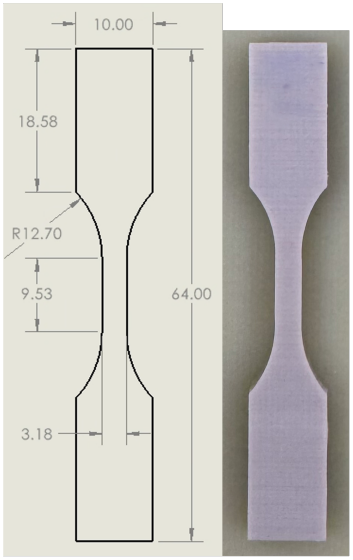


Figure 2.3: Dimensions and appearance of flat and vertical Type V travelers

PEEK extrusion temperatures.

2.2.2 Coupon Extraction

Several coupon material orientations- $B = 0°$, $15°$, $30°$, $45°$ and $90°$- were chosen for testing and are shown in Figures 4.2a, 4.2b, 4.1c, 4.2d, and 4.2e. These angles were chosen due to anticipated exhibition of the extremes of material anisotropy. The $0°$ and $90°$ shows the material orientations in perpendicularity while the in-between angles show the range of elastic and plastic behavior and reveal if there are interactions between the two directions. The use of a large blank allowed both consistent material properties through the height of the coupon and flexibility in extraction configurations.

Inclusion of the orientations of $B = 15°$ and $B = 30°$ was important because at approximately $B = 25.05°$, and as seen in Figure 2.4, the print layers of the coupons critically change from extending the test section height of the coupon to only extending the width. Having multiple layers that span the length of the coupon allows for load path redundancy in the case of inter-layer splitting. Typically, this redundancy also allows for more plastic behavior. When a split occurs on a coupon without the option of several load paths, the break is more abrupt and brittle.

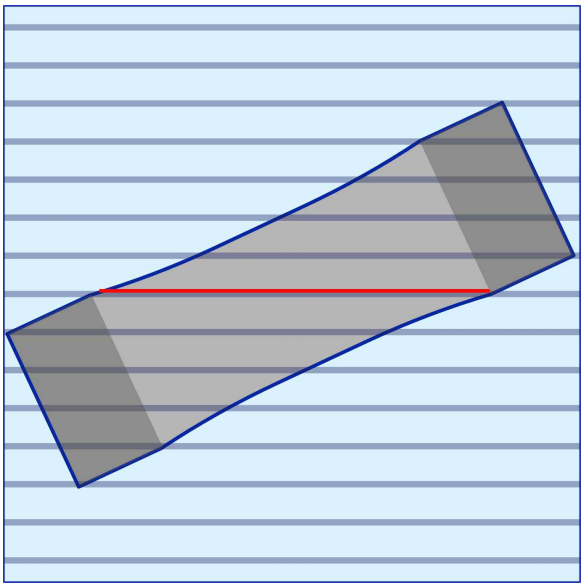


Figure 2.4: The B-angle where fibers just span the coupon test length, $\approx B = 25.05°$

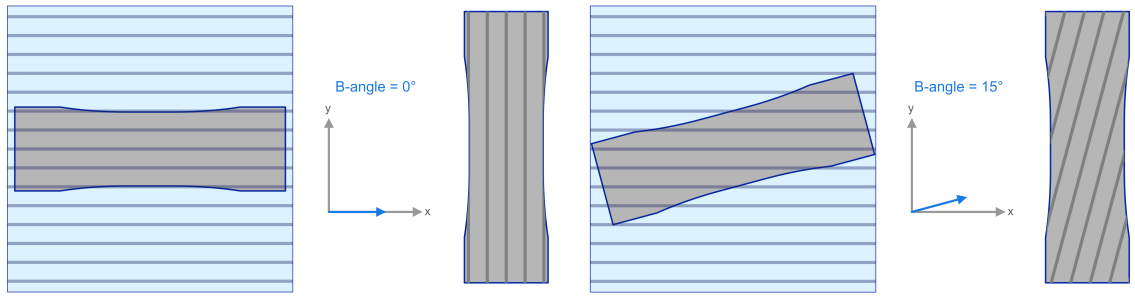
Coupons were extracted from the blanks using a Zund Ultrasonic Router, as seen in the extraction bed in Figure 2.6. The router settings were adjusted to ensure crisp edges and no melting of the material during cutting. The use of this equipment ensured the uniformity and quality of the coupon edges and allowed flexibility in the extraction arrangement. Due to the large width and height of the blanks, multiple coupons or a combinations of coupons and travelers could be extracted from a single blank. Out of 50 PEEK blanks, over 60 wide coupons and 28 vertical ASTM type V traveler coupons were extracted.

2.2.3 End Tab Application

After coupon extraction, the next step in preparation involved ensuring the samples were suitable for accurate testing was the attachment of end tabs, seen in Figure 2.1. End tabs distribute the applied force more evenly across the coupon, especially with a short grip length. End tabs also aid in preventing edge effects from the textured machine grips and ensure that the coupon deforms uniformly during testing. The attachment process included the adhesion of 2.4mm thick Epoxyglass end tabs onto ends of the coupons using JB Weld Epoxy Adhesive. The epoxy was sanded down to be flush with the coupon edge, which helped with vertical alignment within the guides of the instiron.

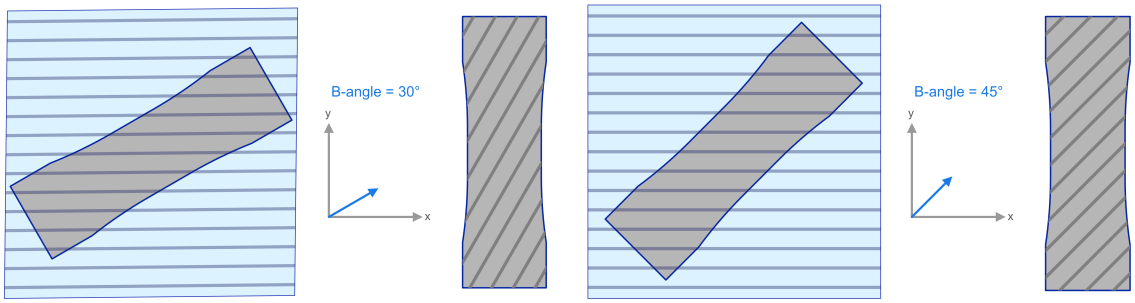
2.2.4 DIC Paper Application

Traditionally, methods for applying DIC speckle patterns have been inconsistent or labor-intensive due to the use of spray paint splatters or time-consuming hand dotting methods. However, in this approach, a DIC pattern is printed onto temporary tattoo paper and transferred to the surface of the test coupon with water. Figure 2.7 shows the coupon before and after speckle tattoo paper application. This method allows for consistent, high-quality pattern application at a custom size most conducive to valuable data collection. By using this method of application, it becomes possible to consistently and efficiently evaluate the full-field strain across the entire surface of the coupon—not just within the central test section.



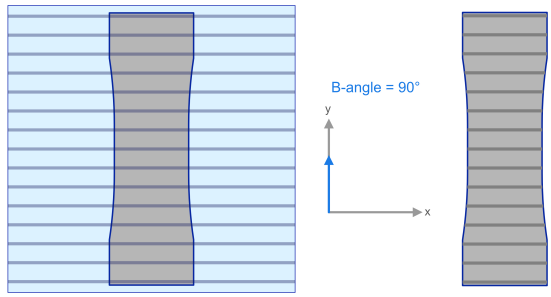
(a) $B = 0°$

(b) $B = 15°$



(c) $B = 30°$

(d) $B = 45°$



(e) $B = 90°$

Figure 2.5: B-angle graphics

2.3 Testing

2.3.1 Setup

The testing was performed on a ShoreWestern Instron tensile testing machine. Each sample was loaded into the grips and tensile force at a constant crosshead speed was applied until

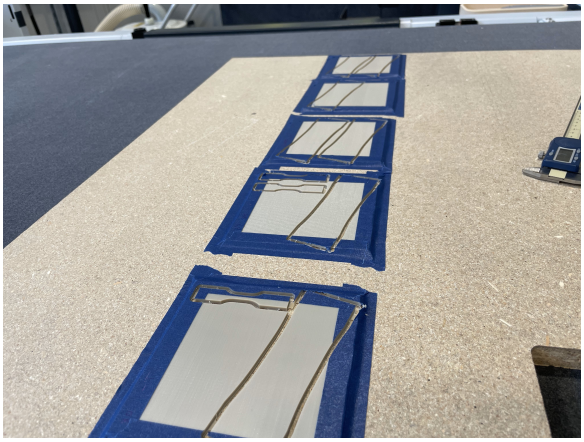


Figure 2.6: Blank prints directly after routing

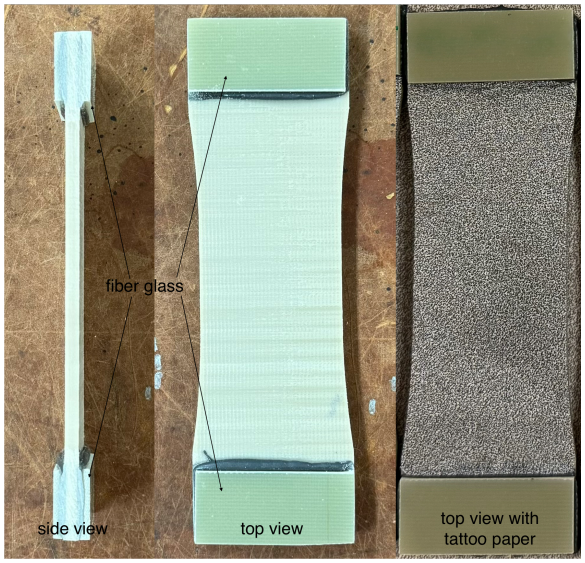


Figure 2.7: Coupon without and with DIC tattoo paper

the coupon fractured. The grip strength was set to ≈ 300 psi, at a cross-head speed of 0.025mm/sec. Concurrent pictures of each sample's DIC surface were taken at 0.5-second intervals. For some additional samples, a high-speed camera was also pointed at the coupon to aid in capturing the point of fracture.

Both the horizontal and vertical travelers were tensile tested without DIC to obtain the

ultimate strength. Having consistent output results from these travelers confirmed consistent print conditions through the duration of production and the validity of comparison between coupons produced at different times.



Figure 2.8: Coupon testing setup

2.3.2 Test Outputs

The tensile testing produced several valuable outputs for analyzing material behavior. Stress-strain curves from the Instron system provided an overview of nonlocalized mechanical properties such as Young's modulus, yield strength, and ultimate tensile strength, as well as insight into the elastic and plastic regimes of response. Images taken during testing were later used for DIC analysis, offering data for full-field strain.

High-speed video captured the real-time progression of deformation and fracture, offering visual insight into failure mechanisms. Additionally, the fractured specimens were inspected after testing, allowing for insight into fracture modes and propagation origins as well as potential material defects and print quality observations within the volume of the coupon.

Chapter 3

MODEL DEVELOPMENT

Several methods of modeling were used to analyze coupon performance. While the commercial software package Abaqus ([[14] was used in coupon geometry development, an in-house MATLAB ([15] Finite Element Analysis (FEA) program was developed to allow easy flexibility in the analysis domain of these specifically oriented tensile tests. An in-house FEA program was developed to serve as a base for custom material property identification processes.

3.1 Transversely Isotropic Model

The compliance matrix for a 3D transversely isotropic material is shown formulaically below, where E_z corresponds to modulus in the direction normal to the print layers (2), and E_p corresponds to the modulus in-plane with the print layers (1,3). Because of the symmetry that comes with transverse isotropy, $\frac{\nu_{zp}}{E_z}$ and $\frac{\nu_{pz}}{E_p}$ are equal, meaning there are only 5 independent variables in consideration.

$$\begin{Bmatrix} \epsilon_{11} \\ \epsilon_{22} \\ \epsilon_{33} \\ \epsilon_{12} \\ \epsilon_{13} \\ \epsilon_{23} \end{Bmatrix} = \begin{bmatrix} \frac{1}{E_z} & -\frac{\nu_{zp}}{E_z} & -\frac{\nu_{zp}}{E_z} & 0 & 0 & 0 \\ -\frac{\nu_{zp}}{E_z} & \frac{1}{E_p} & -\frac{\nu_p}{E_p} & 0 & 0 & 0 \\ -\frac{\nu_{zp}}{E_z} & -\frac{\nu_p}{E_p} & \frac{1}{E_p} & 0 & 0 & 0 \\ 0 & 0 & 0 & \frac{1}{G_{zp}} & 0 & 0 \\ 0 & 0 & 0 & 0 & \frac{1}{G_{zp}} & 0 \\ 0 & 0 & 0 & 0 & 0 & \frac{1+\nu_p}{E_p} \end{bmatrix} \begin{Bmatrix} \sigma_{11} \\ \sigma_{22} \\ \sigma_{33} \\ \sigma_{12} \\ \sigma_{13} \\ \sigma_{23} \end{Bmatrix}$$

The transversely isotropic stiffness matrix, which is used in FEA calculations to determine strains at any point on the coupon surface given the stresses, is the inverse of the compliance

matrix.

3.2 Matlab Code

3.2.1 MATLAB Objective

The MATLAB FEA package allows users to input their own elastic material properties and view predicted coupon behavior and strains in both global and localized strain directions.

3.2.2 Considerations and Input

The MATLAB FEA package includes several options prior to evaluation. The coupon can either have force or displacement controlled evaluation, where the user specifies either the final load applied to the ends or the final displacements at the end. There is also an option to select the application surface for these end conditions. As shown in Figure 3.1, the chosen force/displacement is either applied to the grip surface area, or to only the top and bottom surfaces at the coupon ends. For this evaluation and in correlation with tensile testing, the former makes the most sense, as the grip sections do not experience significant deformation in the tensile test machine, and force is applied in a greater area at the ends than just the top and bottom of the coupon.

The application of force and displacement at the grip necessitates careful consideration of the model's fixity assumptions. It is assumed that only to top grip areas experiences movement in the vertical direction, and any other nodes in this area remain fixed in the x,z, and torsional directions. The test area between the grips, however, is free to move in any direction of moment once force or displacement is applied.

Additional necessary input for FEA evaluation includes elastic material properties, B-angle of the coupon, and number of desired mesh layers through the coupon thickness.

3.2.3 Meshing

The MATLAB program automatically meshes coupons with the chosen dimensions and chosen number of mesh layers through the coupon depth. Shown below in Figure 3.2 are two coupon geometries used in the experiment, but with three different potentials of meshing

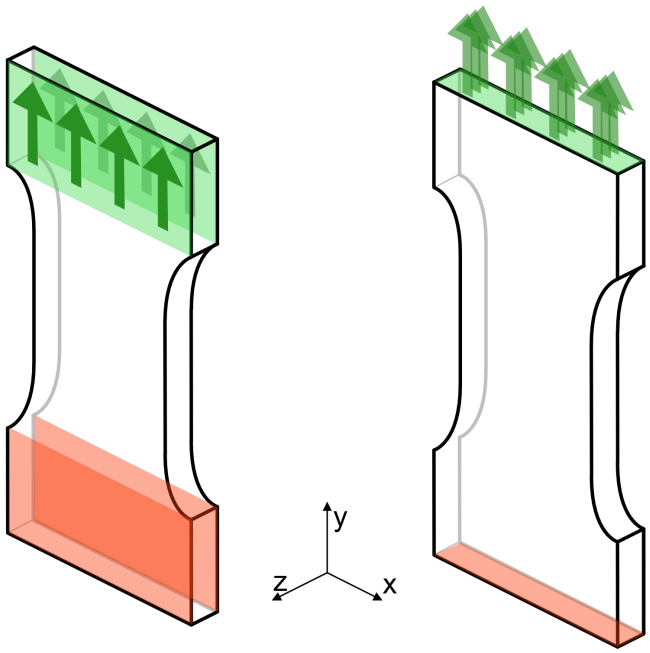


Figure 3.1: Two possible FEA fixity configurations

depending on the user's choices. In these instances, the geometry of the left wide test coupon has one layer of elements through the thickness of the coupon, as does the traveler-sized coupon. The middle image in 3.2 demonstrates a wide coupon with two element layers through the thickness. The element sizes are optimized to be as equal-dimensioned and as close to cubic as possible. To determine the ideal mesh for a coupon, continuous tests should be run until the output strains converge.

3.2.4 Finite Element Analysis

At a generalized level, the following formulation is used for the finite element analysis.

$$[K] = \int_V [B]^T [C][B]\, dx$$
$$\{P\} = [K]\,\{u\}$$

where $[K]$ = the global stiffness matrix, u = displacement and P = nodal forces. $[B]$ is the strain-displacement matrix for each element. The symbolic volumetric integration

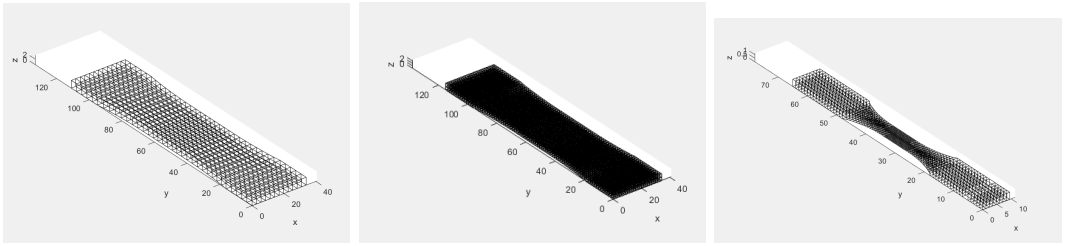


Figure 3.2: One-layer Wide coupon mesh (Left), two-Layer wide coupon mesh (Middle), one-Layer traveler coupon mesh (Right)

for $[K]$ was performed in Mathematica [16]. $[C]$ is the constitutive matrix, and can be transformed for any B-angle using the following rotation matrix for transversely isotropic buildups:

$$\begin{bmatrix} c^2 & s^2 & 0 & 2cs & 0 & 0 \\ s^2 & c^2 & 0 & -2cs & 0 & 0 \\ 0 & 0 & 1 & 0 & 0 & 0 \\ -cs & cs & 0 & c^2 - s^2 & 0 & 0 \\ 0 & 0 & 0 & 0 & c & -s \\ 0 & 0 & 0 & 0 & s & c \end{bmatrix}$$

where c =cos(B-angle) and s =sin(B-angle) Once the formulation for the above equations was completed in Mathematica, the symbolic matrices were translated to Matlab syntax and used in the package.

The same rotation matrix shown above is later used to extract the strain at the necessary local orientation after evaluation. With this package, the user can also select a specific coordinate location and view the closest node's stresses and strains in all 6 degrees of freedom.

3.2.5 FEA Output

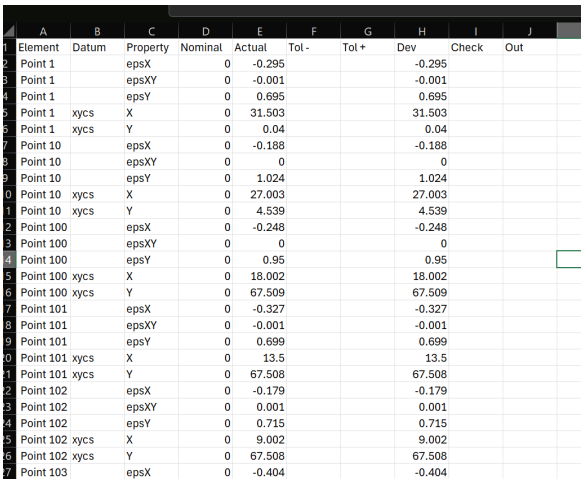
The output plots from the FEA package include plots of untransformed strain in the x and y axes, as well as plots of the transformed strain in the localized material direction.

3.2.6 Future Programming Work- GOM Integration

This program could integrate an error minimization process alongside input DIC data to extract material properties.

To put this material property extraction into effect, csv GOM DIC data (see Figure 3.3) for a coupon within the elastic range is needed, as well as the coordinates at each of those points. The program will begin with a baseline FEA analysis and approximate initial material properties. An initial error of the FEA strains in comparison to the DIC strains will be calculated, and the difference sum between actual and recorded strains begins the error minimization process. With the first derivatives and partial derivatives of the B-matrix for each of the 5 unknown constitutive properties symbolically derived in Mathematica, they can then be used in a Newton-Raphson formulation. By continuing to iterate until the error between the MATLAB output and GOM input is at a minimum, the 5 material properties can then be considered optimized for that particular instance of transverse anisotropy and B-angle.

Portions of this program have already been written towards this error minimization step. The first derivatives and Hessian matrix have been calculated, and a program takes the GOM strain input with coordinates and finds different strain corresponding to the closest node on the FEA output.



	A	B	C	D	E	F	G	H	I	J
1	Element	Datum	Property	Nominal	Actual	Tol -	Tol +	Dev	Check	Out
2	Point 1		epsX	0	-0.295			-0.295		
3	Point 1		epsXY	0	-0.001			-0.001		
4	Point 1		epsY	0	0.695			0.695		
5	Point 1	xycs	X	0	31.503			31.503		
6	Point 1	xycs	Y	0	0.04			0.04		
7	Point 10		epsX	0	-0.188			-0.188		
8	Point 10		epsXY	0	0			0		
9	Point 10		epsY	0	1.024			1.024		
10	Point 10	xycs	X	0	27.003			27.003		
11	Point 10	xycs	Y	0	4.539			4.539		
12	Point 100		epsX	0	-0.248			-0.248		
13	Point 100		epsXY	0	0			0		
14	Point 100		epsY	0	0.95			0.95		
15	Point 100	xycs	X	0	18.002			18.002		
16	Point 100	xycs	Y	0	67.509			67.509		
17	Point 101		epsX	0	-0.327			-0.327		
18	Point 101		epsXY	0	-0.001			-0.001		
19	Point 101		epsY	0	0.699			0.699		
20	Point 101	xycs	X	0	13.5			13.5		
21	Point 101	xycs	Y	0	67.508			67.508		
22	Point 102		epsX	0	-0.179			-0.179		
23	Point 102		epsXY	0	0.001			0.001		
24	Point 102		epsY	0	0.715			0.715		
25	Point 102	xycs	X	0	9.002			9.002		
26	Point 102	xycs	Y	0	67.508			67.508		
27	Point 103		epsX	0	-0.404			-0.404		

Figure 3.3: Example of exported GOM data. The localized normal and shear strains as well as their corresponding coordinates would allow integration with the MATLAB FEA program.

Chapter 4

RESULTS

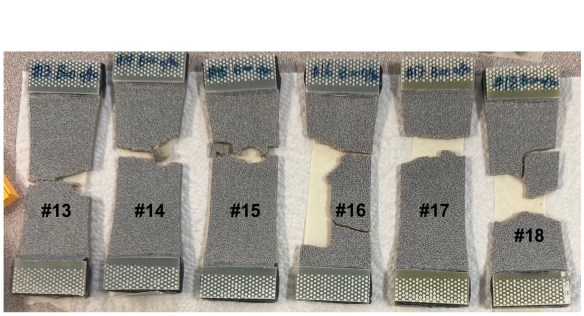
The following chapter begins by presenting and discussing the images of the fractured coupons for both rasters. Next, the elastic curve of the traveler's demonstrate consistent print conditions. Finally, a comprehensive strain analysis plotting method indicates the behavior of all coupons tested.

4.1 Post-Testing Coupon Images

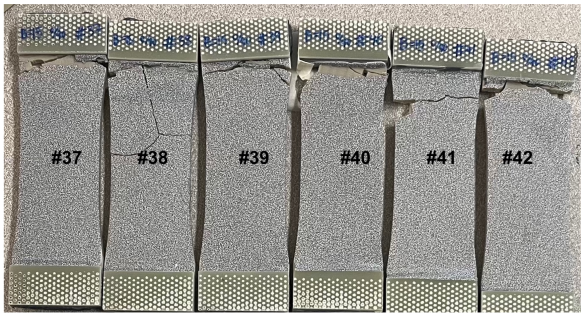
Shown below in Figures 4.1 and 4.2 are images of the coupons post-failure in the [0/90] and [±45]. Six coupons were tested at each B-angle and with both rasters, for a total of 60 coupons.

The coupon images provide qualitative insights about anisotropic behavior of the coupons. For the B=0° coupon, ≈ 300 layers spanned the entire test section length of the coupon. This number gradually reduces with increasing B-angle, with ≈ 130 layers at B=15°. At angles greater than 25.05°, from 2.4, no print layers span the length of the coupon. Coupons under this B-angle were more likely to experience plastic deformation, and development of Lüders bands- localized bands of plastic deformation, which are frequently the source of the majority of the global deformation. The coupons with B-angles greater than 25.05° were more likely to exhibit brittle failure, and deformation primarily within the elastic range. See [2] stress-strain curves resulting from these PEEK experiments. Consistent yield stresses were seen through coupons at each B-angle and raster.

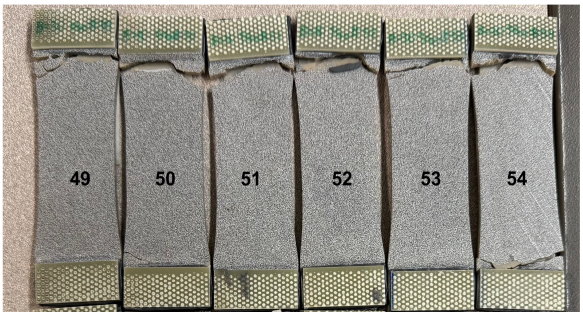
On the $B = 30°$ coupons, the failures occur towards the grip sections of the coupons. As seen in corresponding FEA strain concentrations in 4.3, this is due to the print layers nearly spanning the length of the coupon but failing to do so, and stress concentrates near the grip areas.



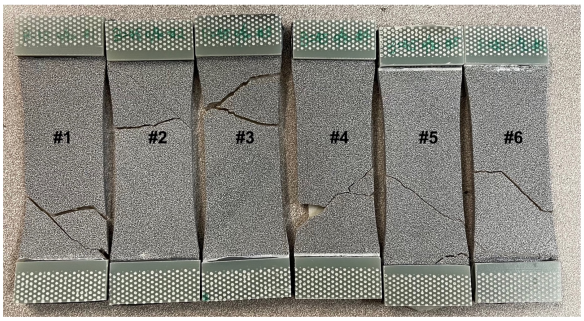
(a) $B = 0°$



(b) $B = 15°$



(c) $B = 30°$



(d) $B = 45°$

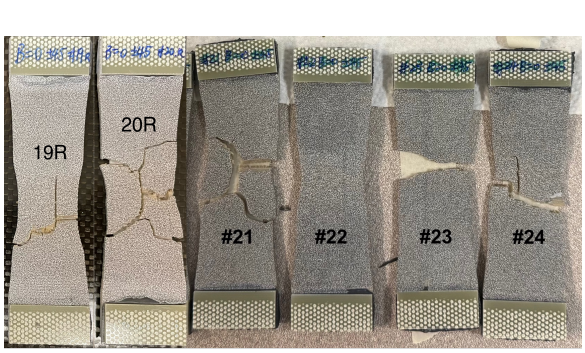


(e) $B = 90°$

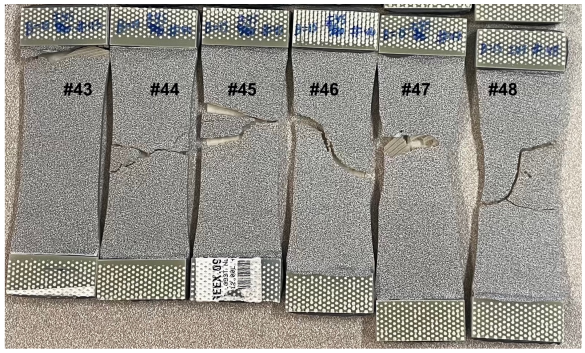
Figure 4.1: All tested PEEK dogbone coupons ([0/90] configuration)

4.2 Printer Consistency Verification

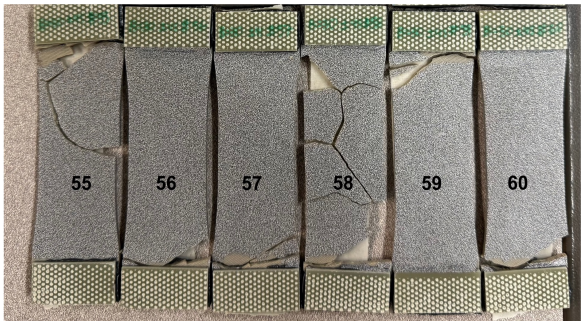
See [2] and Figures 4.4 and 4.5 for traveler coupon curves, shown in Figures . The stress-strain curves associated with these travelers showed consistent strength, indicating steady printing conditions between samples and through the print timeline.



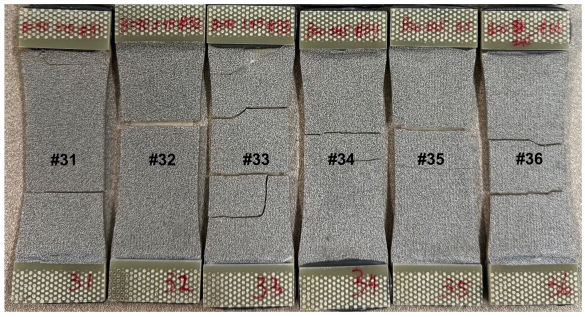
(a) $B = 0°$



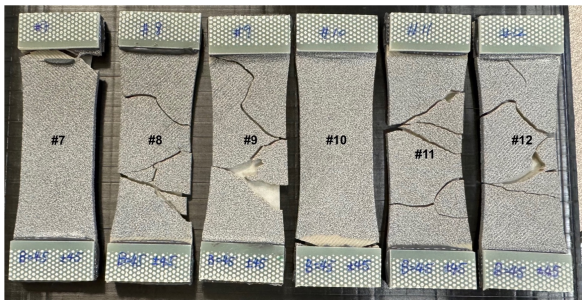
(b) $B = 15°$



(c) $B = 30°$



(d) $B = 45°$



(e) $B = 90°$

Figure 4.2: All tested PEEK dogbone coupons ([±45] configuration)

4.3 Strain and Hotspot Analysis

To establish strain-based failure limits for the materials, the strain data can be examined along the transformed directions perpendicular and parallel to the print layers, denoted by

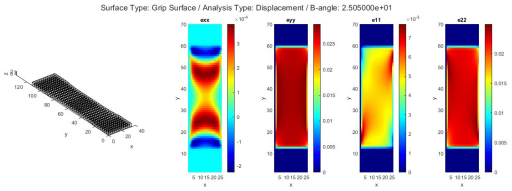


Figure 4.3: $B = 25.05°$ coupon stress concentrations

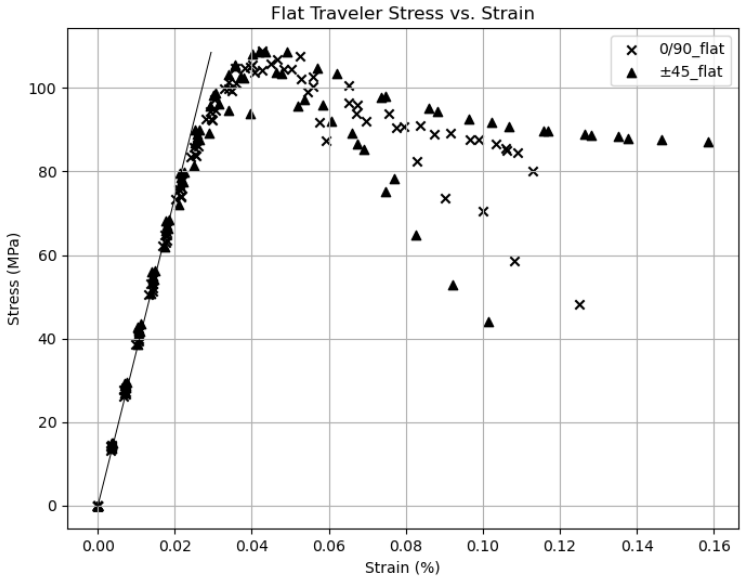


Figure 4.4: Stress-strain curves for all flat travelers

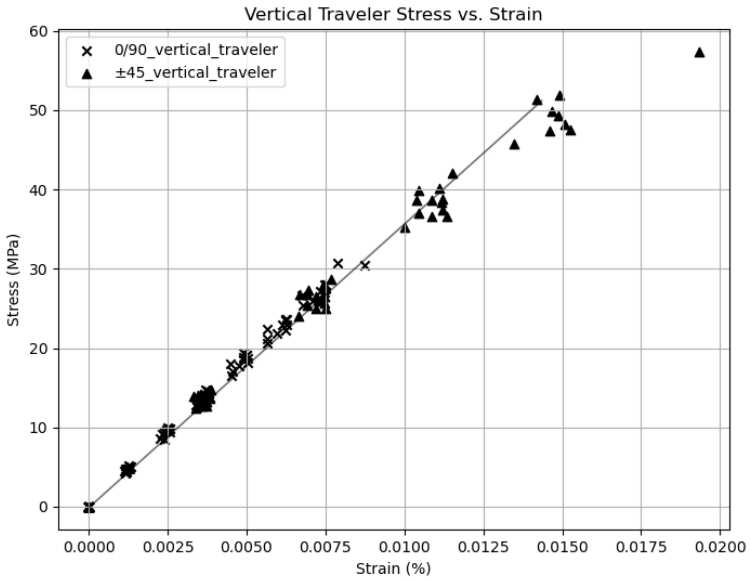


Figure 4.5: Stress-strain curves for all vertical travelers

ϵ_{11} and ϵ_{22}, respectively. This analysis method relies on an assumption of plane strain, where the strain in the directions not measured by testing (through the thickness of the coupon, or what would be 33) is taken to be 0. Due to Poisson effects, strain within the coupon perpendicular to the direction of elongation was likely to be negative as coupons experienced greater positive deformation in the tensile test direction.

4.3.1 Strain Extraction

A semiautonomous process was developed to evaluate coupons, determining both the physical area of and method of failure with minimal user input. This process is also described in Appendix A. With this method, and through GOM Correlate [17], the area of interest on each coupon is narrowed down for higher point density. Figure 4.6 demonstrates the process for defining local coordinates and creating an objective array of points to extract strain.

The resulting data exported out of GOM are strains in the two local directions through-

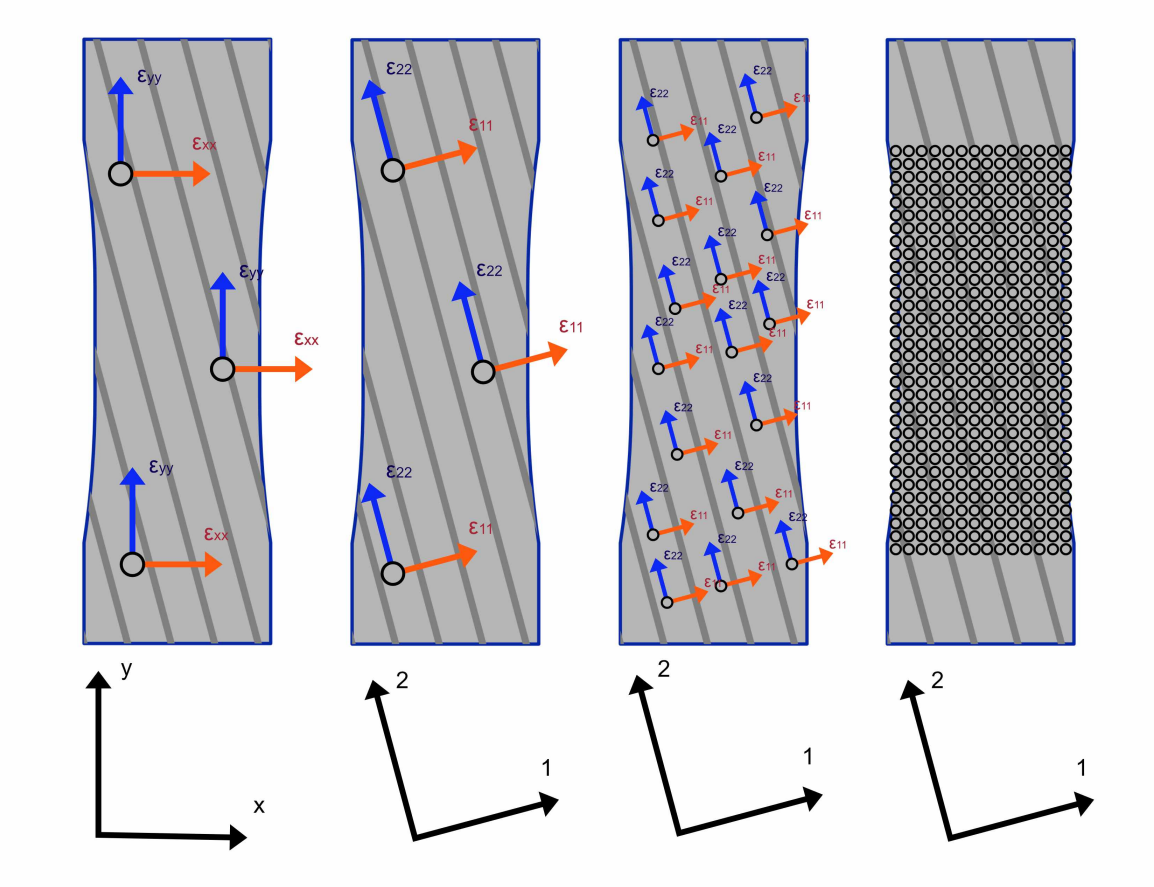


Figure 4.6: Diagrams demonstrating untransformed global strains, transformed local strains, higher discretization of local strains, and extremely dense discretization of local strains, respectively.

out the test duration, typically 700-1000 points on the selected DIC surface area, and 300-1500 strain steps. This results in anywhere between 420,000- 3,000,000 unique strain points per coupon. Along with the localized strain data for these points, the untransformed coordinates are also taken relative to each point to aid in fracture origin examinations. This data, once exported into a CSV and input into the developed MATLAB script, is then run through a series of filters prior to plotting. These filters eliminate noisy data from pictures taken after fracture, as well as points not consistently recognized in GOM due to being on a boundary or having inconsistent lighting. The filters also cancel out noise from areas of

extreme deformation where the DIC data is no longer viable.

4.3.2 Tornado Plotting Process

Each individual coordinate exported from GOM corresponds to two localized strain values at that point for every time step captured, on in each of the ϵ_{11} and ϵ_{22} directions. Plotting the strains in the ϵ_{11} direction on a horizontal axis, and ϵ_{22} on the vertical, results in a line visually tracing the coupon's behavior at that particular point for the test duration.

Completing this process not only for one point, but for all of the DIC points in the area of interest creates a comprehensive view of that coupon's material behavior. These combined trace plots are referred to as "Strain Tornadoes" due to their somewhat erratic and cloud-like appearance. The Strain Tornadoes display the entire coupon surface's strain under tension, and serve to establish a lower bound for strain-based failure limits with respect to local coupon coordinates. Specifically within the MATLAB program, these output plots can highlight the user's selected number of top strains in the ϵ_{11} and ϵ_{22} directions. The ϵ_{11} directions plot top strain traces in warm colors, and ϵ_{22} plots top traces in cooler colors as well as dotted lines. The remaining traces on the coupon's selected area plotted in grey behind the top traces.

4.3.3 Strain Tornado Results

Walking along the horizontal ϵ_{11} axis, any points that have positive values indicate tensile strain of the between print layer (originally z) direction. This is relevant, as tensile strain and separation between layers -or splitting- is a commonly observed mechanism of failure. Negative values along the ϵ_{11} axis are a result of Poisson effects, in which the direction opposite elongation experiences contraction.

Observing data with respect to the vertical ϵ_{22} axis yields a greater upper range of strain values. Positive values on this axis reach as much as 6 times higher than on the ϵ_{11} axis, because the printed plane lines aligned with this direction, and can experience greater plastic deformation. Negative values on this axis are rarely found for points on coupons below $B = 90°$. Like the ϵ_{11} axis, a negative value for ϵ_{22} is likely a result of Poisson effects-

but these negative values are of smaller magnitude in comparison with those found in the ϵ_{11} direction.

Coupon 46 Breakdown

Coupon 46 is used in the following subsection to demonstrate the evaluation process and output. It is a $B = 15°$, $[\pm 45]$ raster sample, exhibiting both elastic and plastic behavior and formed a Lüders band at about 1/3 the way through testing. Looking over 628 time steps (a 314 second-long test), there is an emphasis to examine 3 points on the surface through the specific time steps 1, 200, 416, 601, and 628.

As shown in Figure 4.7, the coupon begins with no strain applied. The "tornado" has not yet begun to form and the coupon has yet to experience any strain, but will fill out the entirety of the empty plot by the end of the test.

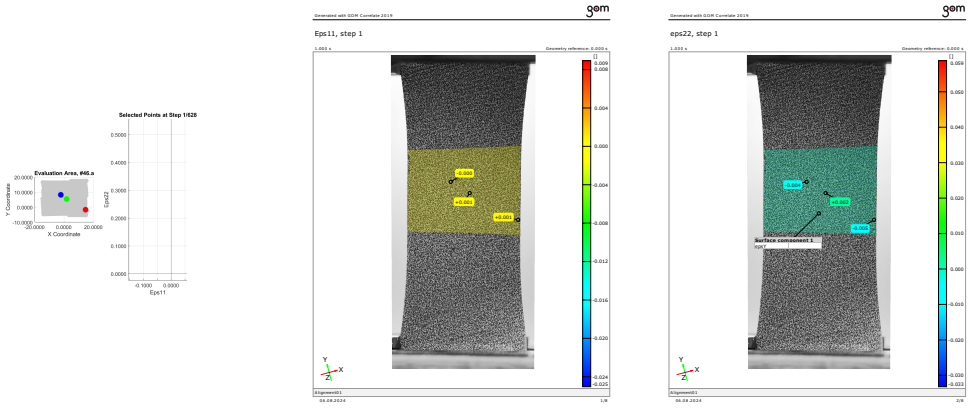


Figure 4.7: Coupon 46 at Step 1.

Next, a force is applied and the coupon deforms within the elastic range. This is shown in Figure 4.8. The 3 emphasized strain lines across the surface of the coupon experience the same strain traces. Note that the DIC output has homogeneity in color, and no concentrations in strain have formed because the test remains in the elastic range. Also of note, approximately 1/3 of the test has been completed with respect to duration, but only

a fraction of the entire strain tornado is completed. This indicates the coupon experienced the majority of its deformation after yielding.

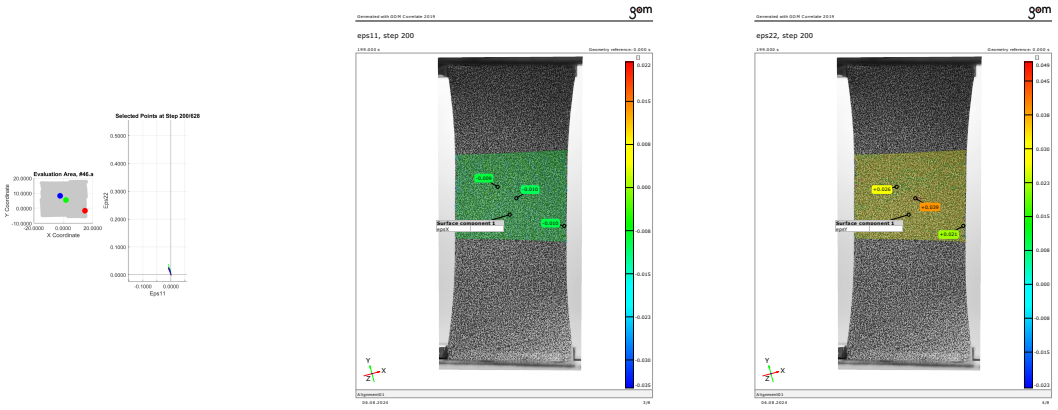


Figure 4.8: Coupon 46 at Step 200.

Once out of the elastic range at step 416, things look a bit different. Shown in Figure 4.9, the two most left points are still following a similar trace. However, the most right point, in red, experiences a more negative value of ϵ_{11} than the other two locations, indicating more contraction in that local direction. This point because it is experiencing an inflection point in the magnitude of negative ϵ_{11}. The coupon has also visibly formed a Lüders band, and has variation of color on the area of the DIC plot, indicating a movement to the plastic deformation range beyond yielding.

At time step 601, as shown in Figure 4.10, all three lines have now deviated from the same trace. The red rightmost point continued on a relatively linear trajectory into quadrant 2, while the other two points continued to grow more in the ϵ_{22} direction. The most left dark blue point is about to cross the $\epsilon_{11} = 0$ axis, and a hotspot is becoming visible in the strain graph.

At step 628, the coupon is one frame from fracture and can be seen in Figure 4.11. The dark blue line has crossed the $\epsilon_{11} = 0$ axis, and the corresponding ϵ_{11} plot shows positive strains all around the region. The green middle point is the greatest value in ϵ_{11}, and remained negative in its ϵ_{11} value. The red and green points indicate two possible types of

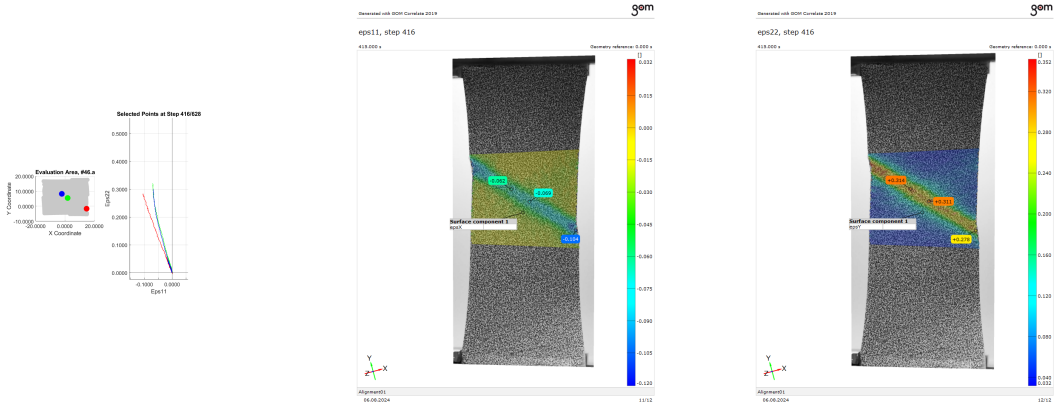


Figure 4.9: Coupon 46 at Step 416.

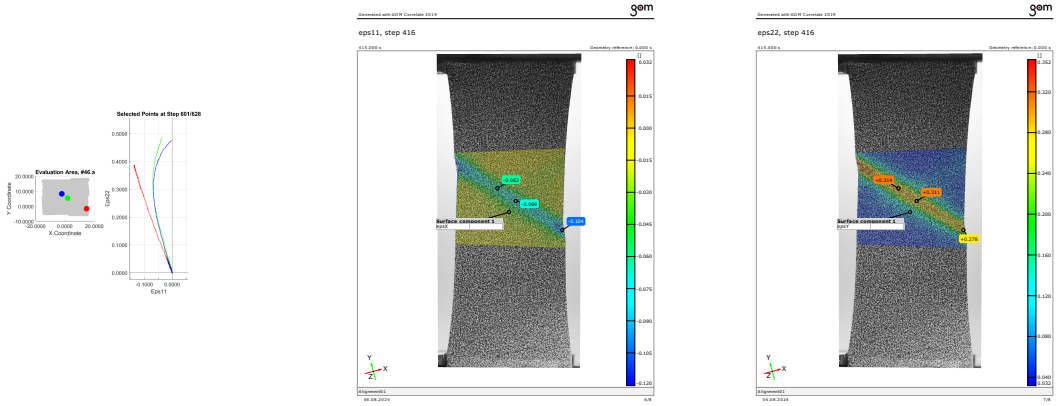


Figure 4.10: Coupon 46 at Step 601.

positive strain failures- an ϵ_{11} failure at about $\epsilon_{11} = 0.05$, or a ϵ_{22} failure at $\epsilon_{22} = 0.505$. Becuase the framerate is only at 2 hz, an ϵ_{11} failure likely initiated and the dynamic response through the coupon caused the entire sample to fail.

4.3.4 All Coupon Tornadoes

Figures 4.17, 4.18, 4.19, 4.20 showcase the strain tornadoes at each B-angle for the [0/90] raster. Likewise, Figures 4.21, 4.12, 4.13, 4.14, 4.15 and 4.16 show the strain tornadoes for

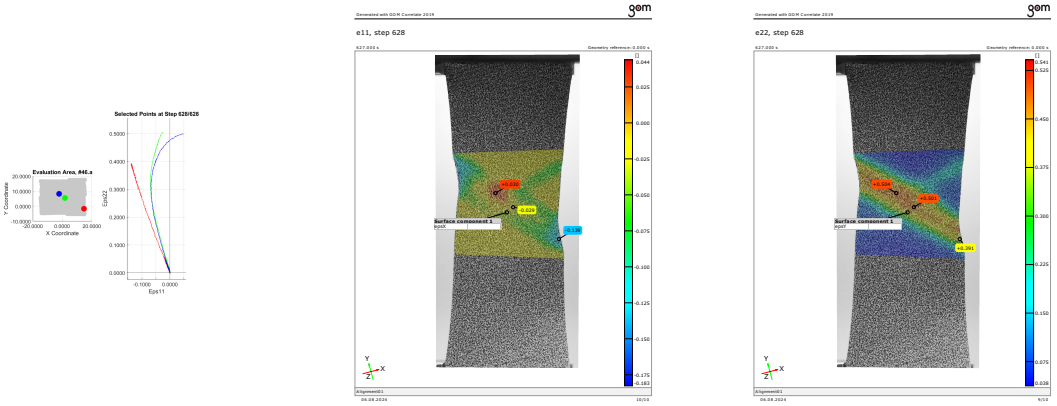


Figure 4.11: Coupon 46 at Step 628.

all of the [±45] rasters.

Shown in Figures 4.22 and 4.21 are the results of plotting the local strains for all B-angle tensile tests in the [0/90] and [±45] raster directions, respectively. Noise for the tests after filtering is more noticeable in B-angles with lower strains ($B = 45°$, $B = 90°$) due to GOM's increment allowance. Based on the assumption that the coupons fail with positive strain in either the ϵ_{11} or ϵ_{22} directions, the envelope for strain limits can be interpreted by looking at the most extreme strain traces in the graph for each point before the entire coupon fractures.

Considering this, the plots demonstrate that the samples of the [0/90] raster had smaller limits overall than the equivalent B-angle samples with [±45] rasters. This is as expected, as the filament lines of the ± 45 coupons are at 45° and never have fibers completely perpendicular to the tensile test. This difference in overall strength comes out to be a 9% difference in the ϵ_{11} direction and a 12% difference in the ϵ_{22} direction.

4.4 FEA Output and Discussion

Shown below in Figures 4.23, 4.24, 4.25,4.26, and 4.27 are the FEA outputs for the elastic properties of [±45] raster derived in [2], under 5mm of displacement from a simulated crosshead. The left part of the image displays the deformed mesh of the coupon, which is

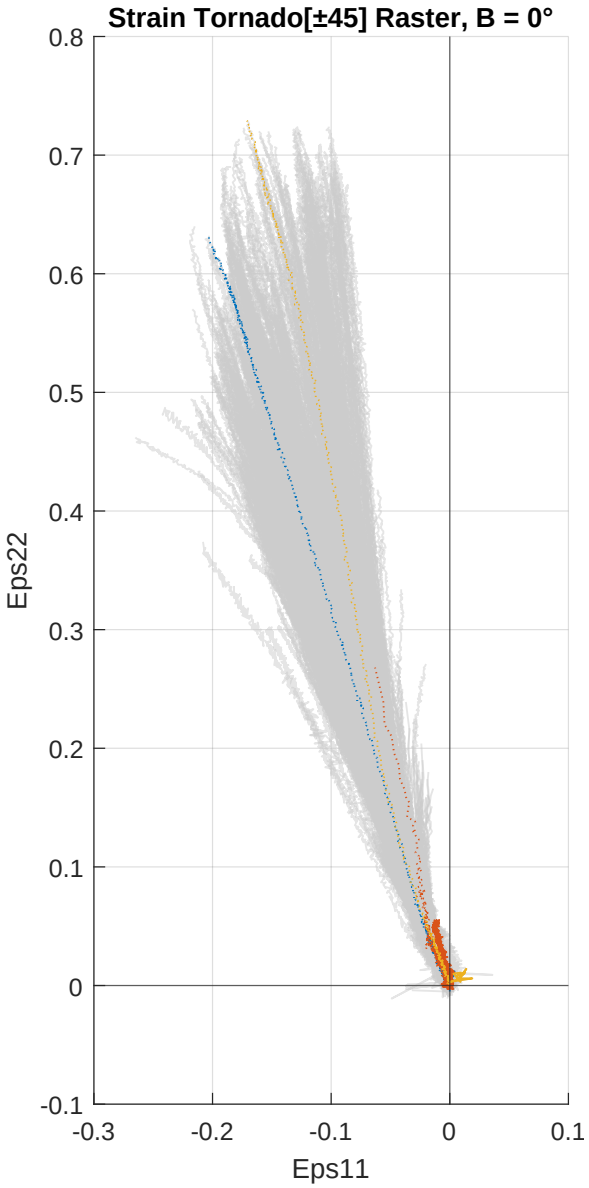


Figure 4.12: [±45] Raster, $B = 0°$ Tornado

rotatable in the output window of the program. The first two plots, from left to right, are the nonlocalized strains of ϵ_{xx} and ϵ_{yy}. The next two plots demonstrate the localized strains in ϵ_{11} and ϵ_{22}.

The strain of ϵ_{11} is at its lowest at $B = 0°$, and highest at $B = 90°$, as would be expected

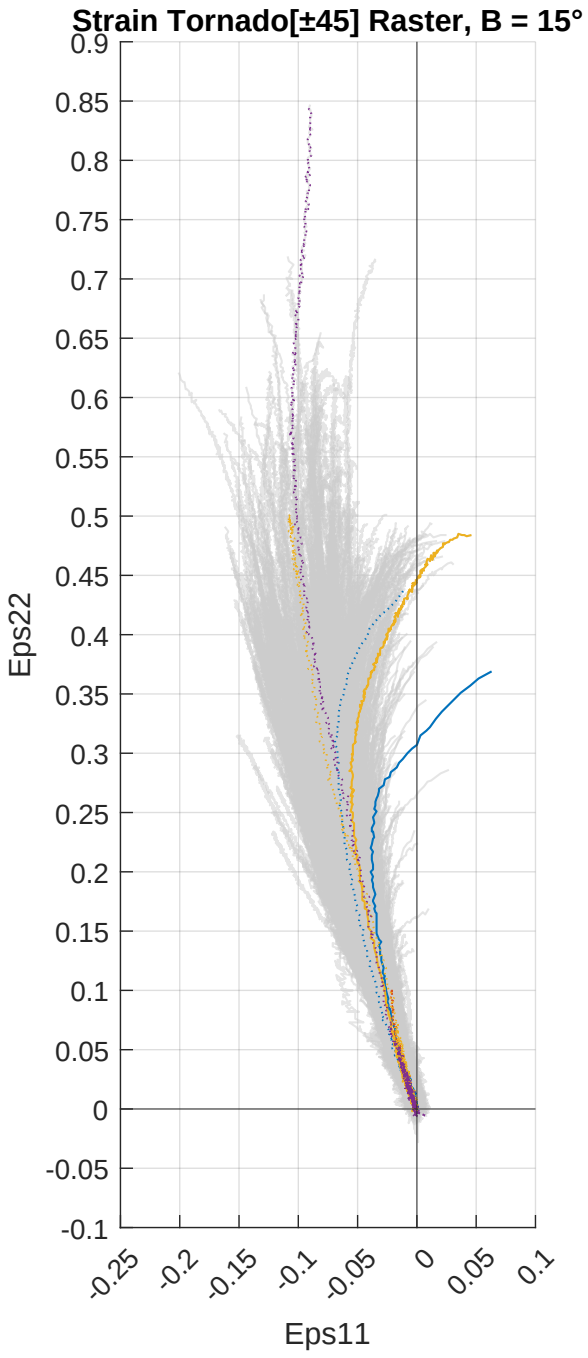


Figure 4.13: [±45] Raster, $B = 15°$ Tornado

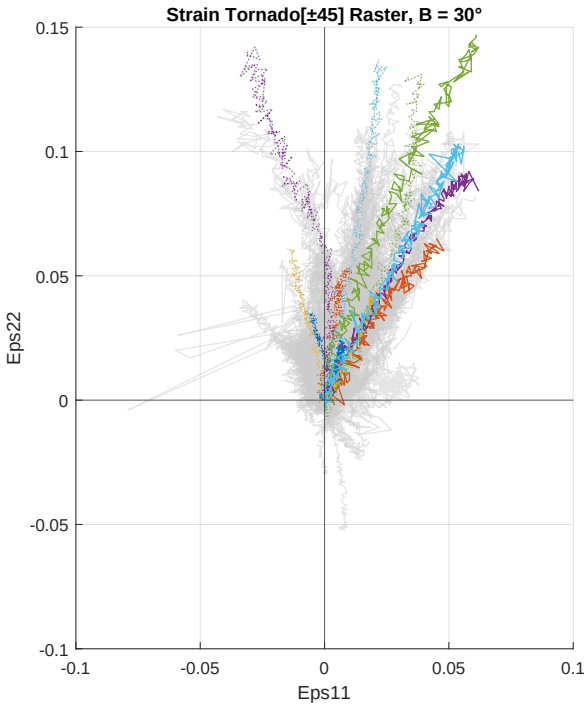


Figure 4.14: [±45] Raster, $B = 30°$ Tornado

considering the anisotropy. The highest strain concentrations are typically at the corners, a function of both where layer lines cross the coupon, and fillet stress concentrations. The entire ϵ_{11} surface appears red for the higher B-angles, leaving the entire surface susceptible to the brittle failure observed at differing areas of the coupons for the $B = 90°$ tensile tests.

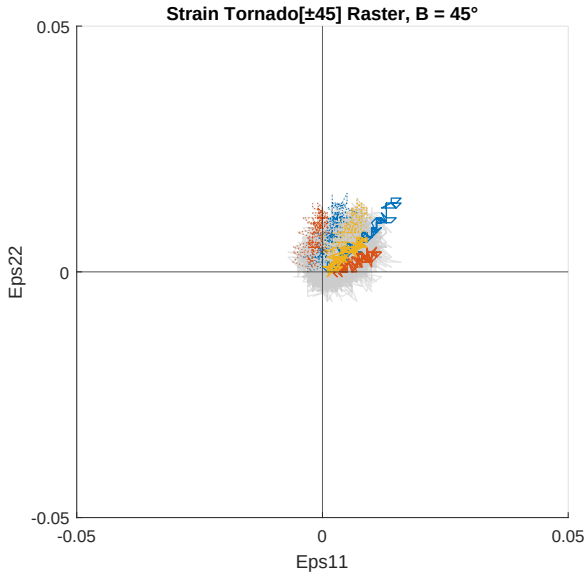


Figure 4.15: [±45] Raster, $B = 45°$ Tornado

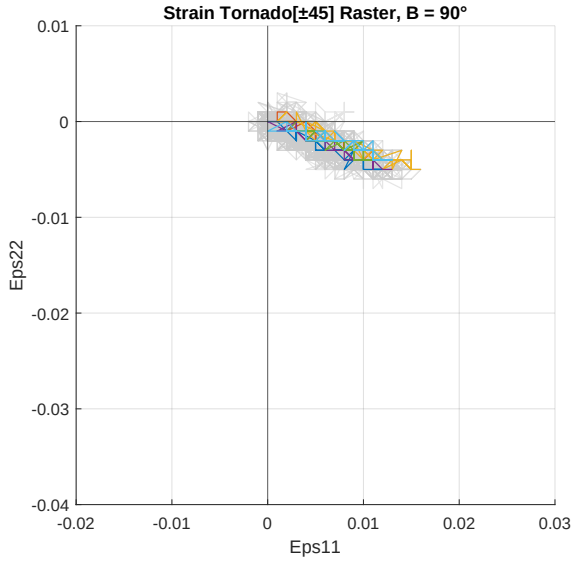


Figure 4.16: [±45] Raster, $B = 90°$ Tornado

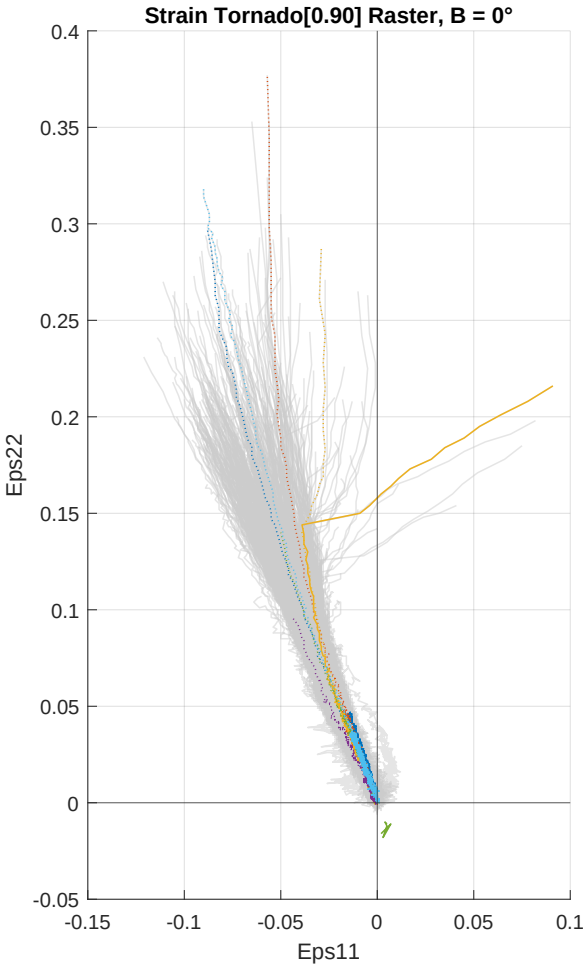


Figure 4.17: [0/90] Raster, $B = 0°$ Tornado

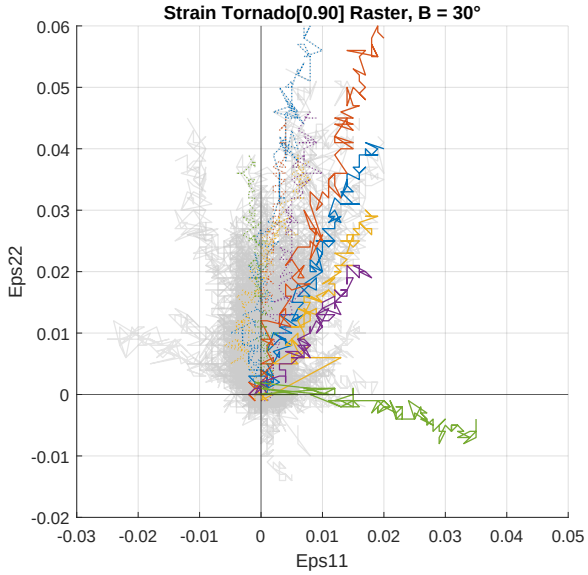


Figure 4.18: [0/90] Raster, $B = 30°$ Tornado

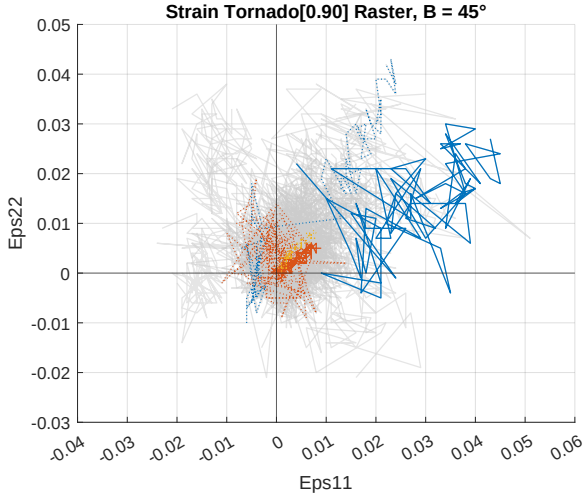


Figure 4.19: [0/90] Raster, $B = 45°$ Tornado

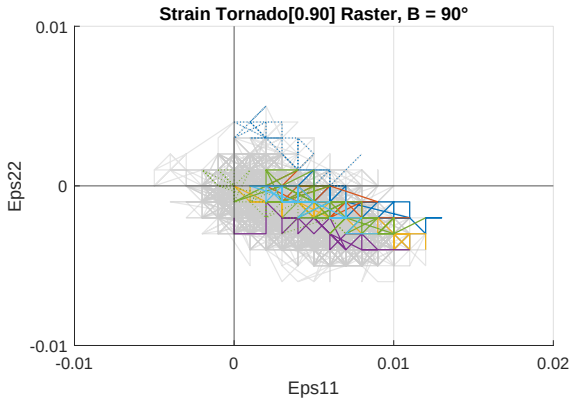


Figure 4.20: [0/90] Raster, $B = 90°$ Tornado

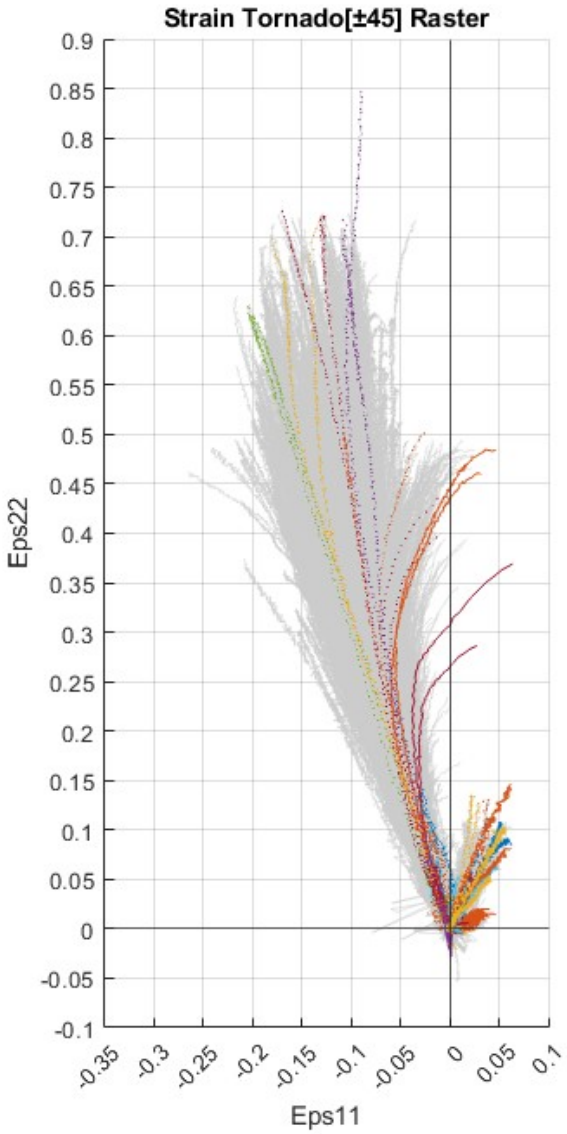


Figure 4.21: Strain Tornado for all ±45 Coupons

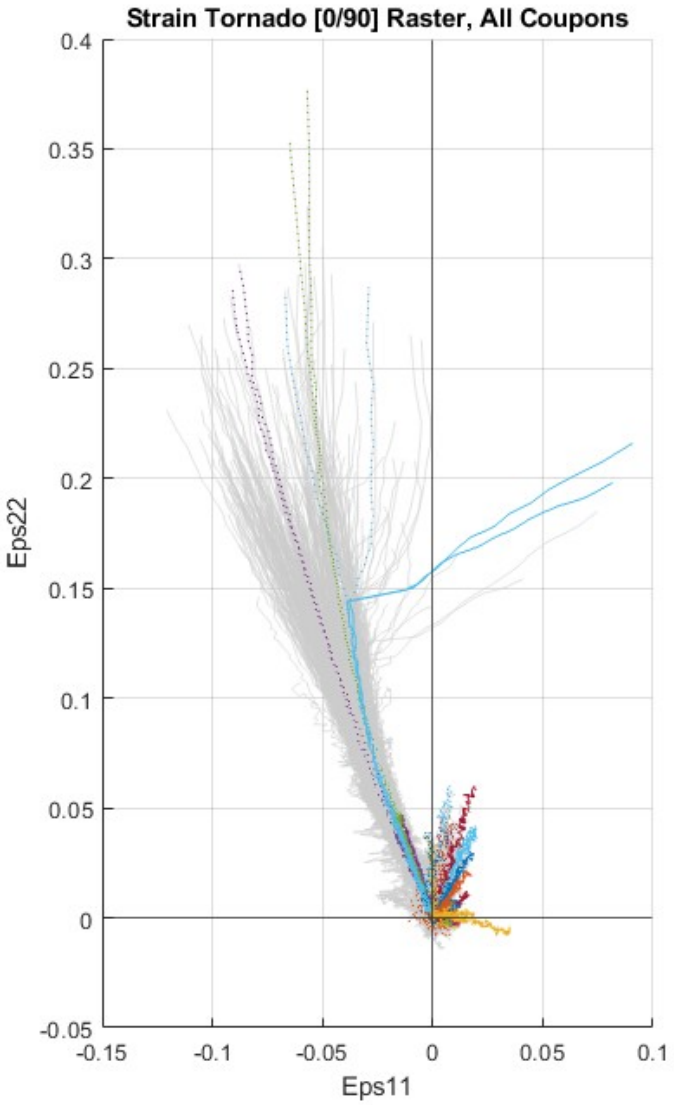


Figure 4.22: Strain Tornado for all 0/90 Coupons

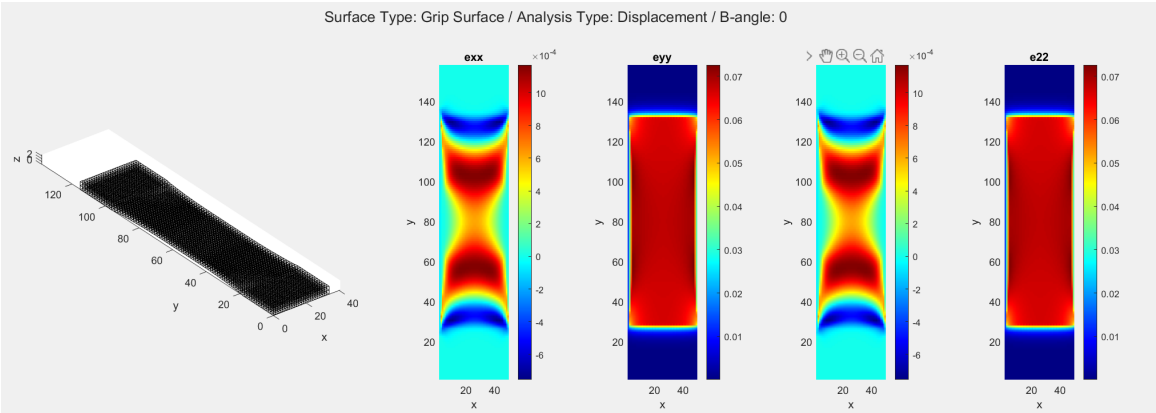


Figure 4.23: Sample FEA output for $B = 0°$

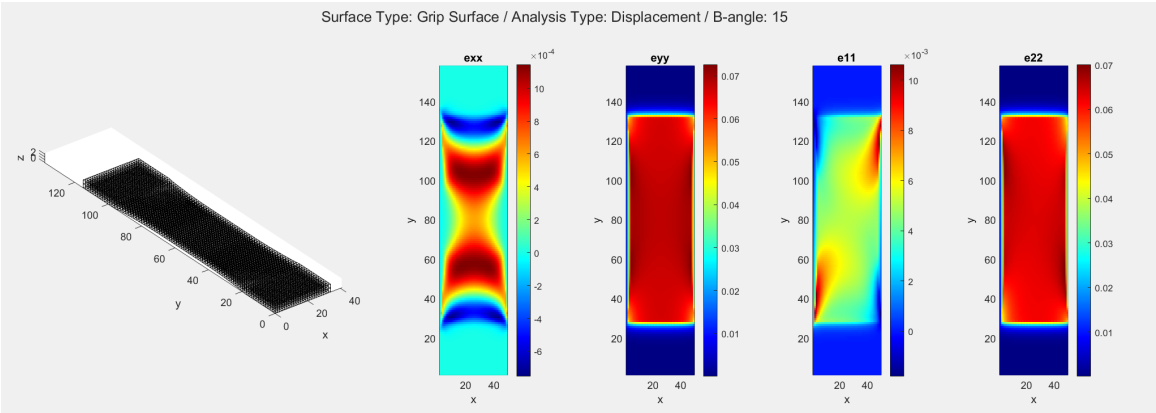


Figure 4.24: Sample FEA output for $B = 15°$

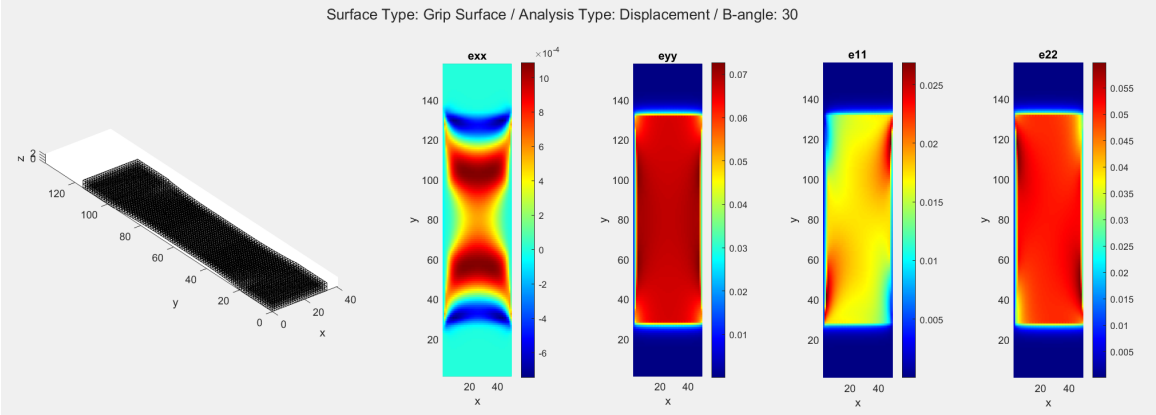


Figure 4.25: Sample FEA output for $B = 30°$

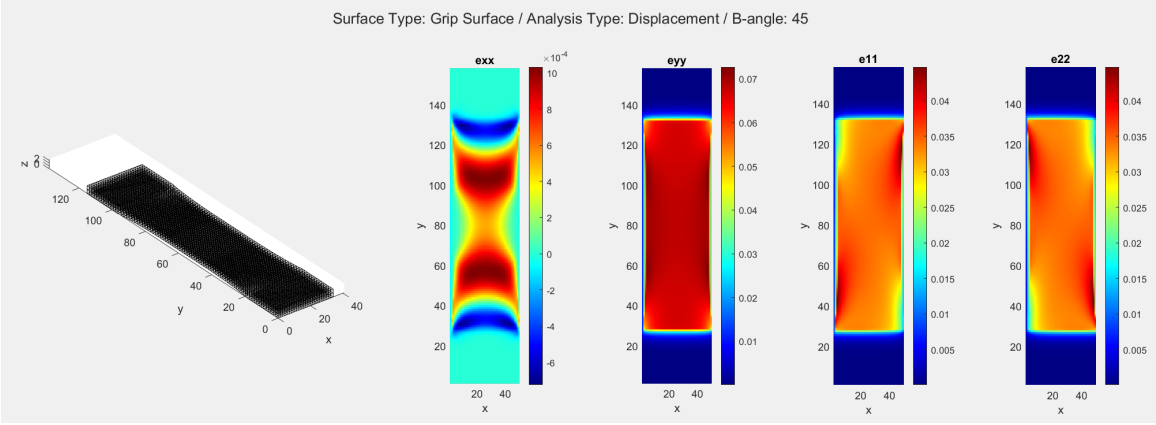


Figure 4.26: Sample FEA output for $B = 45°$

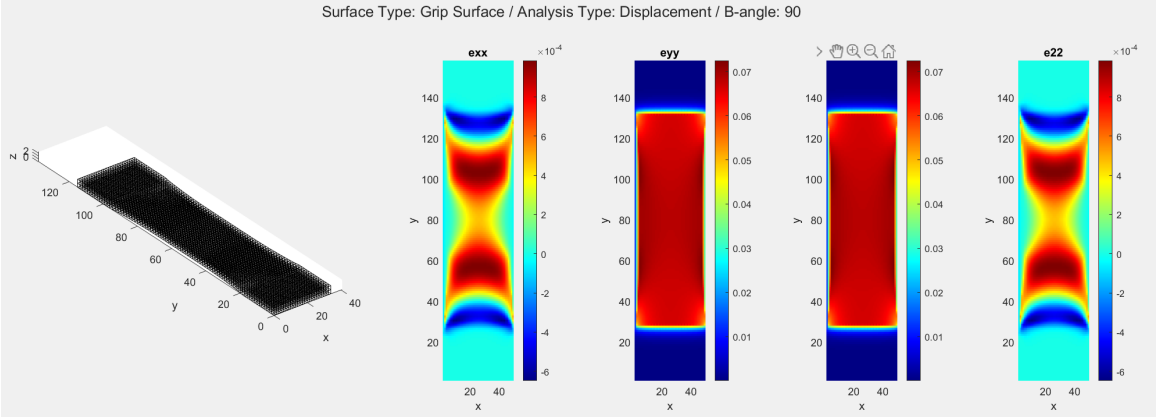


Figure 4.27: Sample FEA output for $B = 90°$

Chapter 5

CASE STUDY

5.1 Motivation

Material properties have been previously theorized [2], and strain limits observed in Section 4.3.4. To validate these findings, additional print configurations and geometries were manufactured and tested. Flexural 3-point bending tests were conducted to assess whether the observed strain limits hold under different loading conditions.

5.2 Design

Geometries for additional specimens were devised to test the elastic and failure properties of the material. Calculations for these beams considered material properties from [2], strain limits from Section 4.3.4, minimizing filament usage, and print constraints such as minimum web and flange thicknesses to ensure a sufficient number of layers (taken to be 3mm).

The finalized printed geometries are shown in Figure 5.1. In addition to the samples exhibiting typical wide flange beam geometry seen on the left side of the figure, simple prisms were also printed as seen on the right. The geometry needed to theoretically initiate failure in the 22 direction is shown in Figure 5.2, but proved to use upwards of 10x more filament than the optimized geometry for the samples failing in the 11 direction so these specimens were not produced.

5.3 Experimental Process

Printing conditions for these samples were kept consistent with those described in Section 2.2.1 and [2]. The initial specimens produced were tested and evaluated using DIC (sample seen in Figure 5.3 in addition to the measurements output by the flexural test apparatus. A second round of testing employed the use of a high speed camera to help specify the origin of samples' fracture. Outputs from the test include stress-strain curves and DIC

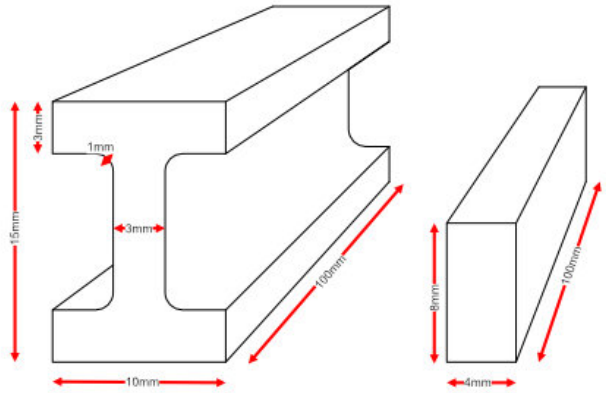


Figure 5.1: Dimensions of the beam and prism used for the case Study

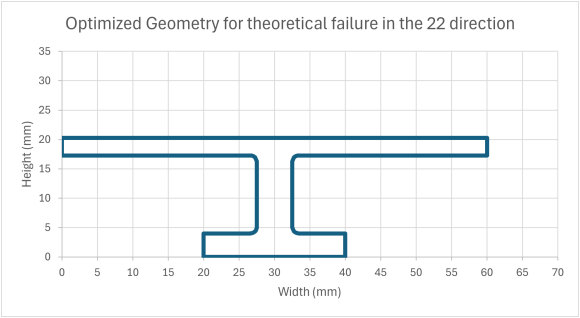


Figure 5.2: Theoretical cross section geometry needed for a failure due to established ϵ_{22} strain limits.

measurements from pictures taken at 0.5 second intervals through the test period.

5.4 Results

[±45] Beams

Before observing the strain tornado fror the [±45] beams, recall these raster's strain limits were 0.06 and 0.72 for the ϵ_{11} and ϵ_{22} directions, respectively. Figure 5.4 shows the viable strain tornadoes output for the [±45] prisms. Designed to fail in ϵ_{11}, several of the traces



Figure 5.3: Beam with DIC y-coordinates highlighted (pre-load)

approach or go past this limit, but none of the traces for any sample come close to the 0.72 limit set for ϵ_{22}. This indicates the developed strain limits may have held for these samples, and the designs failed in the intended directions.

Additionally, the elastic curves for the [±45] beam rasters can be seen in Figure 5.5.

5.4.1 [0/90] Beams

The DIC Strain Tornadoes for [0/90] beam rasters are shown in Figure 5.7. This combined tornado tells a different story than the [±45] raster shown in the previous section. Many of the beams in this raster experienced extreme plastic deformation rendering the strain limits invalid. Of the resulting traces, it appears to far exceed the established strain limits of 0.02 and 0.29 in ϵ_{11} and ϵ_{22}, respectively. The elastic curves for the [0/90] beam rasters can be seen in Figure 5.7. The outlying beam on this plot experienced atypical slipping then splitting.

5.4.2 Discussion

The variation of results warrants an evaluation of process. In particular, an increase of the prism section depth would have encouraged less plastic deformation before failure.

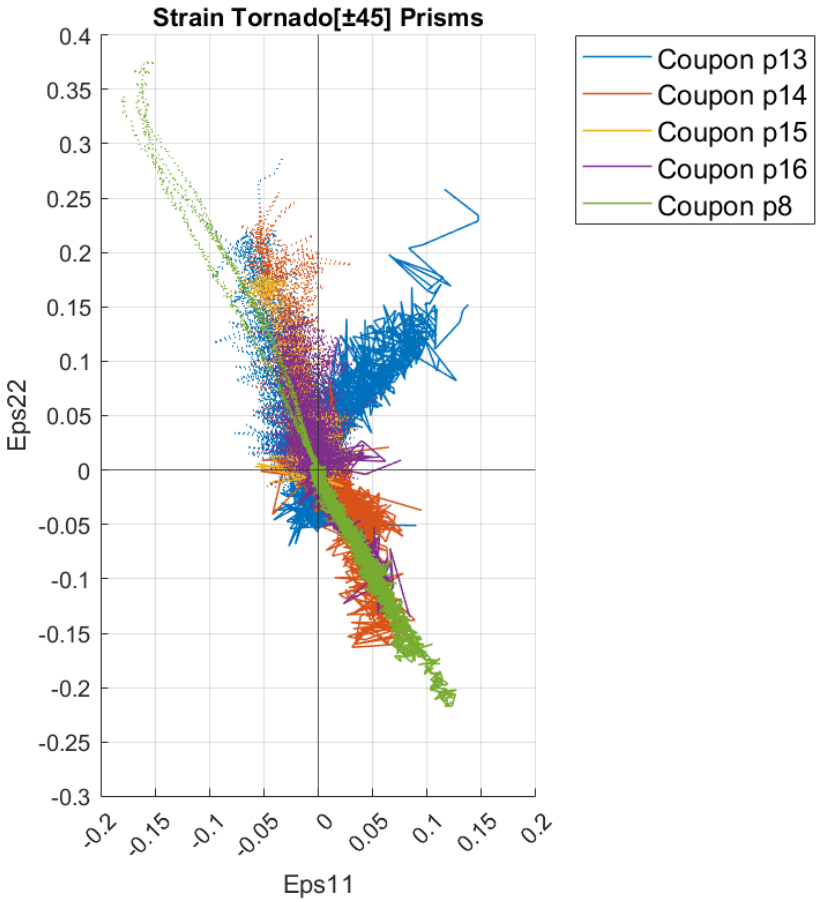


Figure 5.4: Strain Tornado for [±45] prisms

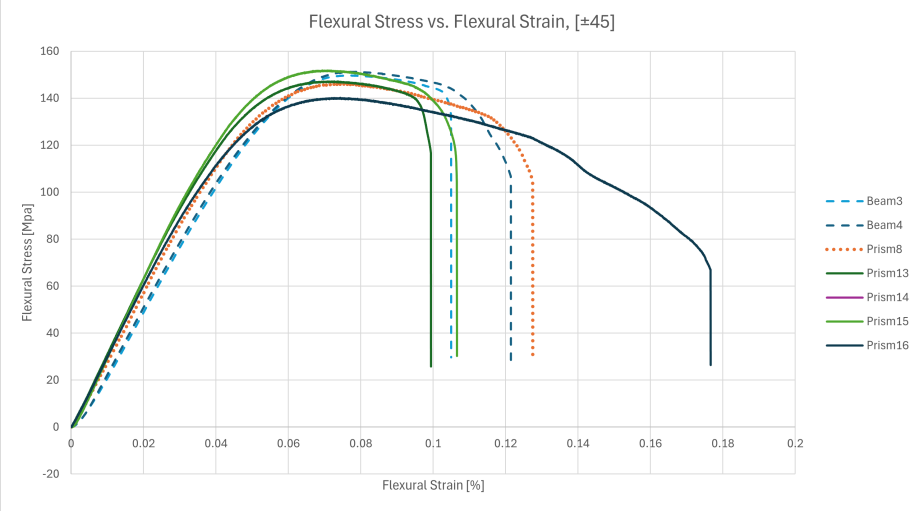


Figure 5.5: Flexural stress-strain curves for the [±45] beams and prisms

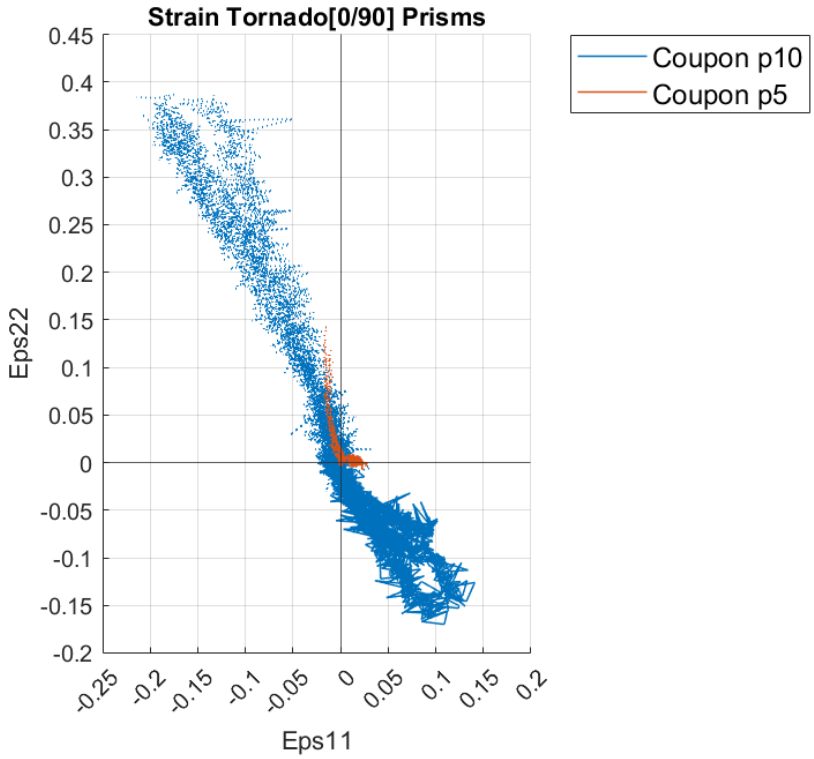


Figure 5.6: Strain tornado for [0/90] prisms

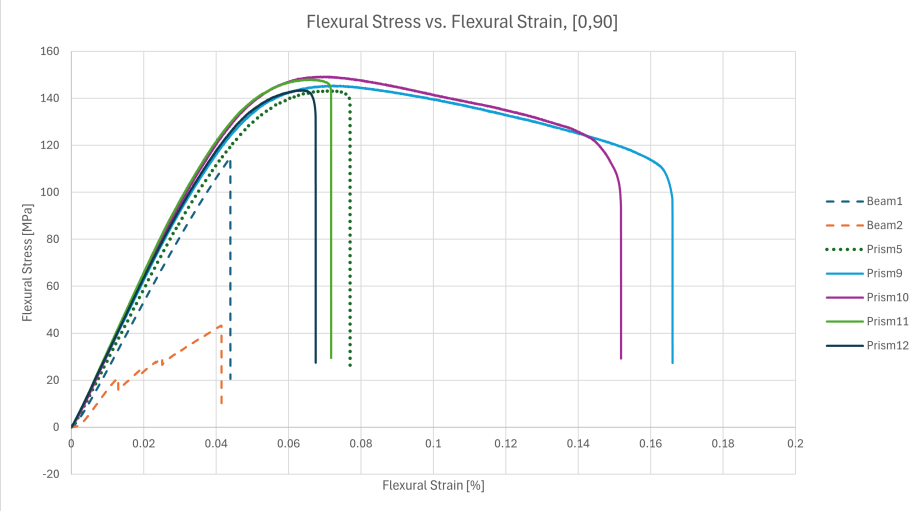


Figure 5.7: Flexural stress-strain curves for the [0/90] beams and prisms

Chapter 6

FUTURE WORK

6.1 Study Expansion

This study could be expanded to capture increasingly comprehensive recordings of coupon behavior, allowing greater confidence in future designs. If the number of angles observed was increased, the tornado envelope would be more complete. Knowing exactly what happens between, for example, $B = 26°$ and $B = 29°$ could prove to be critical for a specific design, and it would not be possible to predict the exact behavior without more information as the current study requires interpolation to assess these values.

The type of testing could also be further expanded upon. Currently, only tensile testing has been completed, but flexural tests, compact tension tests, torsional tests, and compression tests would allow greater material insight and explore behavior in additional dimensions, not just on the 1/2 surface.

6.2 3D Strain Tornadoes

In addition to adding more angles to the strain tornadoes, a third axis could be added, an example of which can be seen for Coupon 46 in Figure 6.1. This would be for the ϵ_{12} direction- the shear strain on the coupon's surface. The addition of this axis would reveal the complete behavior on the coupon surface, and indicate if shear deformations contribute to the coupon's failure. The code has been written to integrate this change, but more data needs to be exported out of GOM. The resulting 3d plots require navigating a 3d GUI, and also are computationally expensive to render and view.

6.3 Geometry Expansion

The original study in 2021 of this PEEK examination looked into bracket-style geometries, recording the failure of varying rasters when broken at the corner of the bends. To proceed

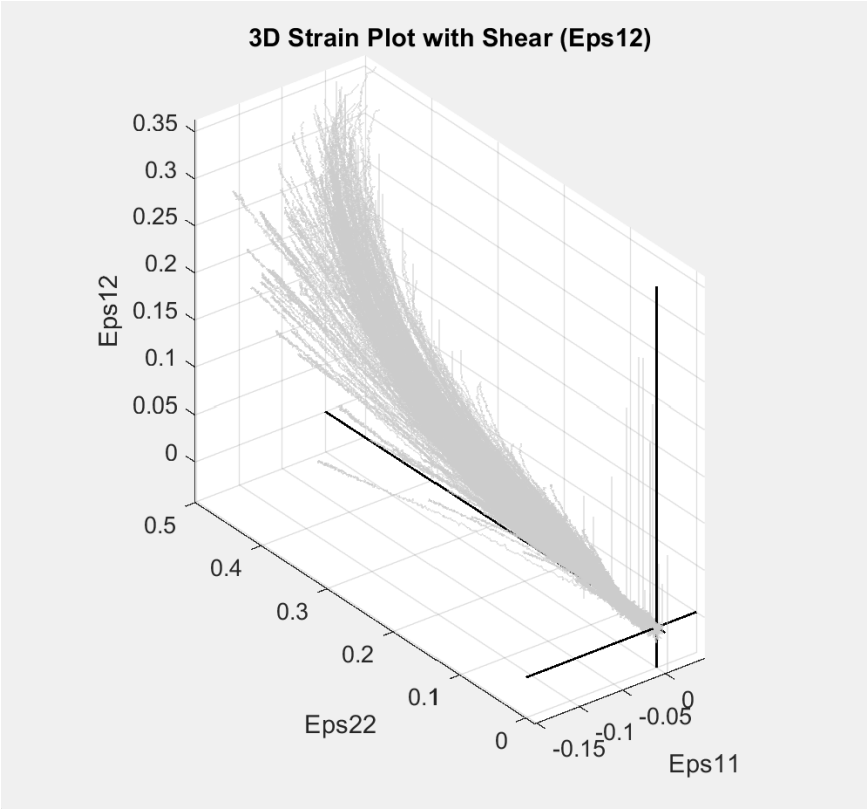


Figure 6.1: 3d Strain Tornado for coupon 46

with characterization, additional geometries could be produced and tested. Using the same DIC data failure analysis and characterization methods on additional shapes has potential for new failure method examinations, as well as to observe whether the strain limits hold with other geometries.

BIBLIOGRAPHY

[1] A. Lingua, N. Piccirelli, D. Therriault, and M. Lévesque. In-situ full-field measurements for 3d printed polymers during mode i interface failure. *Engineering Fracture Mechanics*, 269:108483, 06 2022. doi: 10.1016/j.engfracmech.2022.108483.

[2] J. Lu. Static response and failure prediction of anisotropic material extrusion polymer parts. M.S.. Dissertation, ProQuest Dissertations & Theses, 2024. Available via ProQuest.

[3] D. Popescu, A. Zapciu, C. Amza, F. Baciu, and R. Marinescu. Fdm process parameters influence over the mechanical properties of polymer specimens: A review. *Polymer Testing*, 69:157–166, 08 2018. doi: 10.1016/j.polymertesting.2018.05.020.

[4] P. K. Penumakala, J. Santo, and A. Thomas. A critical review on the fused deposition modeling of thermoplastic polymer composites. *Composites Part B: Engineering*, 201: 108336, 11 2020. doi: 10.1016/j.compositesb.2020.108336.

[5] K. M. Rahman, T. Letcher, and R. Reese. Mechanical properties of additively manufactured peek components using fused filament fabrication. In *Volume 2A: Advanced Manufacturing*, page V02AT02A009, Houston, Texas, USA, 11 2015. American Society of Mechanical Engineers. doi: 10.1115/IMECE2015-52209.

[6] V. Gupta, D. M. Kulkarni, V. V. Chaudhari, N. I. Thiruselvam, and S. Suraj. Investigating the mechanical properties of 3d printed poly-ether-ether ketone (peek) polymer using digital image correlation (dic). *Interactions*, 245(1):352, 11 2024. doi: 10.1007/s10751-024-02187-3.

[7] A. Sabik, M. Rucka, A. Andrzejewska, and E. Wojtczak. Tensile failure study of 3d printed pla using dic technique and fem analysis. *Mechanics of Materials*, 175:104506, 12 2022. doi: 10.1016/j.mechmat.2022.104506.

[8] T. J. Gordelier, P. R. Thies, L. Turner, and L. Johanning. Optimising the fdm additive manufacturing process to achieve maximum tensile strength: a state-of-the-art review. *Rapid Prototyping Journal*, 25(6):953–971, 06 2019. doi: 10.1108/RPJ-07-2018-0183.

[9] S. Mahmood, A. J. Qureshi, K. L. Goh, and D. Talamona. Tensile strength of partially filled fff printed parts: experimental results. *RPJ*, 23(1):122–128, 01 2017. doi: 10.1108/RPJ-08-2015-0115.

[10] W. Szot and M. Rudnik. Effect of the number of shells on selected mechanical properties of parts manufactured by fdm/fff technology. *Advances in Materials Science*, 24(1):86–103, 03 2024. doi: 10.2478/adms-2024-0006.

[11] J. M. Chacón, M. A. Caminero, E. García-Plaza, and P. J. Núñez. Additive manufacturing of pla structures using fused deposition modelling: Effect of process parameters on mechanical properties and their optimal selection. *Materials & Design*, 124:143–157, 06 2017. doi: 10.1016/j.matdes.2017.03.065.

[12] Y. Zhao, Y. Chen, and Y. Zhou. Novel mechanical models of tensile strength and elastic property of fdm am pla materials: Experimental and theoretical analyses. *Materials & Design*, 181:108089, 11 2019. doi: 10.1016/j.matdes.2019.108089.

[13] V. Pagliarulo, P. Russo, G. Leone, G. A. D'Angelo, and P. Ferraro. A multimodal optical approach for investigating 3d-printed carbon peek composites. *Optics and Lasers in Engineering*, 151:106888, 04 2022. doi: 10.1016/j.optlaseng.2021.106888.

[14] Dassault Systèmes. *Abaqus 2024*. Dassault Systèmes, Providence, RI, USA, 2024. https://www.3ds.com/products-services/simulia/products/abaqus/.

[15] The MathWorks Inc. *MATLAB version: 24.1.0.2537033 (R2024a)*. The MathWorks Inc., Natick, Massachusetts, 03 2024. https://www.mathworks.com.

[16] Inc. Wolfram Research. *Mathematica version 14.3*. Wolfram Research, Inc., Champaign, Illinois, 2025. https://www.wolfram.com/mathematica.

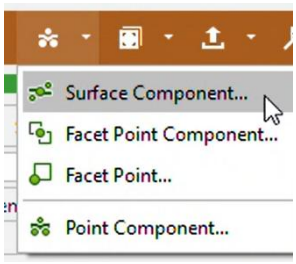
[17] GOM GmbH. *GOM Correlate*. GOM GmbH, Braunschweig, Germany, version 2019 edition, 2019. https://www.gom.com.

Appendix A

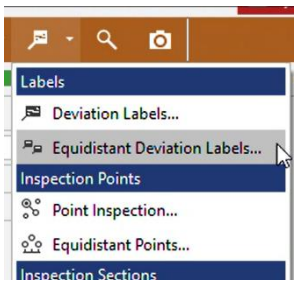
APPENDIX A: GOM STRAIN EXTRACTION

Steps to evaluate coupon in GOM Correlate 2019

1) Test coupons, obtain set of images as testing occurs. These images should be sequentially numbered (can include MATLAB code to rename files) and can include as many images post breakage as needed- no need to trim off. These images should also be oriented so that the pull direction is directly vertical. Make note of the B- Angle and its directionality.
2) Create a new GOM file.
3) Drag and drop all of the test images into the center of the screen and select deformation image out of the two options listed in the pop-up.
4) Dimensionalize coupon by using  button. Select two points of which the distance between them is known. For these coupon samples, the consistent dimension used was the 34mm spanning the grip sections of the coupon.
5) Create a surface component. This step can vary depending on the user, but there are two ways in which this step was done during this project:



   a. Create a surface area over the entire visible coupon surface. This method is fairly straightforward and will capture activity through the surface of the coupon, albeit in a less dense fashion. Simply click Create and Close.
   b. Create a surface area over just a desired portion. If the coupon yields or has an obvious section of breakage, the surface area can be constricted to just the range of this activity to get a denser selection of evaluation points later. Before completing the surface component, click this icon on the bottom taskbar  . Use ctrl + click to create the boundaries of your surface component. Scrubbing along the steps of the coupon is available outside of the specific boundary selection window (press esc or rclick to exit) and is useful to determine specific areas that should be evaluated. Click Create and Close when satisfied with the specific boundary.
6) Now we will create the coordinates for the coupon. Go down the levels of drop-down menus on the left-hand side and click the name of the surface component. One the bar containing the name is selected and greyed, we will create out inspection components. Go under the inspection tab, then Check Dimensions > Positions > Check X > X… and press OK in the pop up. Repeat the process for Y. Now the surface component has been “inspected” for these coordinate values.
7) Create Equidistant Deviation Labels. These are the points in which our inspection components will measure and record specific values. First, navigate the levels of the left-hand side drop down under Part > Inspection > Surface Comparisons > Surface Component Analysis and click to highlight with grey the inspection value you wish to create points for. Then, click the icon shown to induce the pop-up window. GOM has limits as to how many points should be created, so this point distance should be as small as possible to maximize the number of points available for evaluation while still being creatable. In the PEKK and PEEK evaluation point distance was specified to



be the smallest 1/100th place. Click Create and Close once satisfied with allowable point distance and density.

8) Use this same point distance to create points for the Y component. The point distance should not need to be adjusted to create the same number of points.
9) Now we will confirm our points are created and exportable. Under the + Open Tab option on the middle screen division, add Table. This should show all of the deviation points we have created. On the top right of the table tab, make sure the option for 'Values' is selected, rather than Overview or Details.
10) Export Table contents and save as a csv. For the coordinates, save the file as "couponnumber" +'xy', and for the strains simply name the csv as "coupon number", i.e. 35xy and 35 or Fish5xy and Fish5. Make note of the file save location and keep it consistent for later MATLAB evaluation.
11) Delete the deviation labels previously created for the X and Y coordinates. This keeps the computation fast and clarifies exported files for later evaluation.
12) Repeat steps 6 through 9 for the coupon strains. The value to be used in step 6 is under Inspection > Check Dimensions > Strains > Check Epsilon (X) > Epsilon (X).
13) Before exporting the strains, we must perform a coordinate transformation. This is not necessary for coupon angles of B=0, for all others it is necessary for later and consistent evaluation. To transform the coordinates*, go into Operations > Alignment > Manual Alignment > Set Matrix. If the 1 direction (perpendicular to the layers) lies between 90 and 180 degrees, transform the y-direction box to 180. This is to keep all x and y directions between 0 and 180.
14) Perform step 10 for the strains.
15) Proceed to the MATLAB evaluation step

*if the file contains more than ~300 images, coordinate transformation can take considerable time.